Title
Characteristics of Graphitic Films for Carbon Based Magnetism and Electronics

Author
Hong, Jeongmin

Publication Date
2009

Peer reviewed|Thesis/dissertation

UNIVERSITY OF CALIFORNIA
RIVERSIDE

Characteristics of Graphitic Films for Carbon Based Magnetism and Electronics

A Dissertation submitted in partial satisfaction
of the requirements for the degree of

Doctor of Philosophy

in

Mechanical Engineering

by

Jeongmin Hong

December 2009

Dissertation Committee:
Dr. Sakhrat Khizroev, Chairperson
Dr. Qing Jiang
Dr. Cengiz Ozkan

The Dissertation of Jeongmin Hong is approved:

_____

_____

_____

Committee Chairperson

University of California, Riverside

Acknowledgment

First of all, I would like to give my deepest gratitude to my dissertation advisor Dr. Sakhrat Khizroev for his guidance, inspiration, and encouragement through my Ph.D. study. Without his help, it would not have been possible for me to finish this dissertation. He gave me endless support I cannot describe as words for this project and my life.

I would like to give my appreciation to Dr. Robert C. Haddon who gave me advices and instructions on this project. I would like to thank Dr. Qing Jiang and Dr. Cengiz Ozkan who are my committee members. They gave me a lot of advices and directions for this project. I would like to give my thanks to Dr. Elena Bekyrova and Dr. Mikhail Itkis. Their professional research attitude influenced me throughout my graduate study. I thank to Dean's distinguished fellowship awards to be stable to study at UCR for whole graduate study.

I would like to express my gratitude to all of my group members for their time during many discussions with me. I thank friends in Bourns College of Engineering for their cooperation and help on this project. I thank staffs in ME, EE departments, and CNSE administration office and clean room for their time for training, help, and advices in a variety of facilities in clean room.

I am grateful to all of my friends in California, New York, Korea, and all other places around the world for their continuous support to me. I would like to thank my parents and parents-in-law: Seongik Hong, Yesook Choi, Woo-Saeng Lee and Soonhee Park and other family members in Korea for their endless support for me and my family.

Finally and very importantly, I would like to give my deep appreciation to two most important people: my wife, Sookhyun Lee and my son, Ryan Laewon Hong. Their patience, encouragement, and love have continuously given me the courage to face the many challenges that arose in pursuit of my Ph.D. degree.

To my wife, Sookhyun Lee and my son, Ryan Laewon Hong

ABSTRACT OF THE DISSERTATION

Characteristics of Graphitic Films for Carbon Based Magnetism and Electronics

by

Jeongmin Hong

Doctor of Philosophy, Graduate Program in Mechanical Engineering
University of California, Riverside, December 2009
Dr. Sakhrat Khizroev, Chairperson

This dissertation concentrates on the characteristics of graphene, a single layer of graphite, defined as two-dimensional material for carbon based magnetism and electronics. Carbon materials, which are demonstrated by diamond and graphite, have always been of great interest for their unique properties. Moreover, in the last two decades, there have been three revolutionary milestones in the development of carbon materials, which were related to the discovery of fullerenes, carbon nanotubes, and graphene, respectively. Such research evolution led to the realization of the feasibility to tailor magnetic and electronic properties of graphitic sheets.

Magnetism of carbon materials is of particular interest because of its new and relatively unexplored origins. The technological potential of the new materials is enormous as they promise to become the first room-temperature ferromagnetic

semiconductors – the Holy Grail of the world of electronics. Not to mention that the existence of the new materials is vital for the emerging field of spintronics. Researchers believe that new carbon-based magnetic materials could greatly extend the limits of current technologies relying on magnetic and semiconducting properties. In this work, the magnetic properties of pristine graphene and chemically modified graphene were mainly investigated. The chemical functionalization with nitrophenyl (NP) groups was performed by covalent attachment of aryl groups to the basal plane of carbon atoms. The functionalized samples were found to be in a mix of ferromagnetic and antiferromagnetic states with spins aligned in the main plane at room temperature.

Based on these findings, this work attempted to identify the origins of the intrinsic magnetism and potential ways to tailor magnetism in graphene. Such technology has great potential to pave a way to the next-generation technologies containing high-speed and high-density nonvolatile memory as well as the production of reconfigurable logic devices, integrated magneto-optical devices, quantum information devices, and many others.

CONTENTS

LIST OF TABLES

LIST OF FIGURES

1. Introduction

1.1 Motivation

Since the 1960s, when the fabrication of semiconductors became a viable enterprise, the semiconductor industry has developed into the form of an aggregate of companies engaged in the design and fabrication of semiconductor devices. While the size of the semiconductor industry has greatly expanded from that time, the dimensions of the transistors it produces have shrunk significantly - seven orders in size and fourteen orders in areal density - in accordance with Moore's Law, which was identified by Gordon Moore, the co-founder of Intel.

Over the past 50 years, the semiconductor industry has greatly obeyed Moore's Law as shown in Figure 1-1. The typical linear dimension of a feature on an integrated circuit decreases in size by a factor of two around every 18 months [1]. In 2009, Intel provided an updated roadmap of future processors based on their Westmere family of CPUs, which are manufactured using the 32-nm manufacturing process. Intel expects that the processor that it anticipates releasing in 2010, which it has codenamed Sandy Bridge, will be manufactured using 22-nm manufacturing process.

Depending on the doubling time used in the calculations, this could mean up to a 100-fold increase in transistor count per chip within a decade. The current roadmaps for semiconductor industry technology predict a three-year doubling time for microprocessors, leading to a 10-fold increase in the next decade [2]. Intel has reported

that assuming favorable economic conditions, the downsizing of silicon chips will continue over the next decade [3] and will persist through 2029 [4].

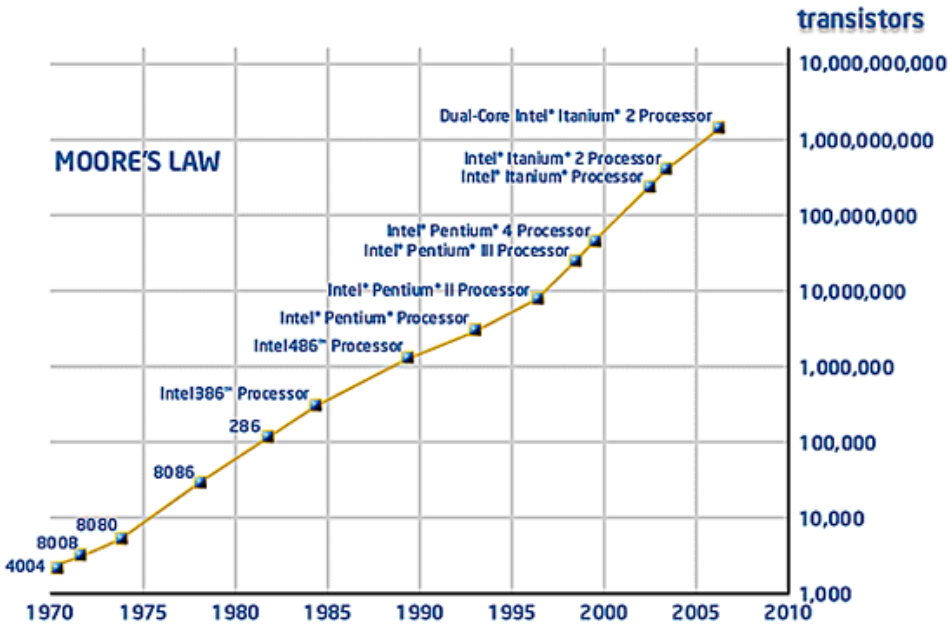

Figure 1-1 Moore's Law.

Despite the significant development of the semiconductor industry, it is now facing the challenge of Metal Oxide Semiconductor Field Effect Transistor (MOSFET) based silicon industry when the size of a transistor reaches the order of a few nanometers. As shown in Figure 1-2, conventional transistors have three terminals: the source, the drain, and the gate electrode. The source and drain are connected by a channel that is composed either N doped (P-type MOSFET) or P doped (N-type MOSFET) semiconductor material. The gate electrode is composed of a layer of polysilicon- placed over the

channel but separated from the channel by a thin layer of insulating material, such as silicon dioxide. When voltage is applied between the gate and source terminals, the electric field generated penetrates through the oxide and creates an “inversion layer” below the oxide. Because the inversion layer is of the same type (P-type or N-type)- as the source and drain, it provides a channel through which current can pass. Varying the voltage between the gate and the source modulates the electron density of this layer and makes it possible to control the current flow between the drain and the source.

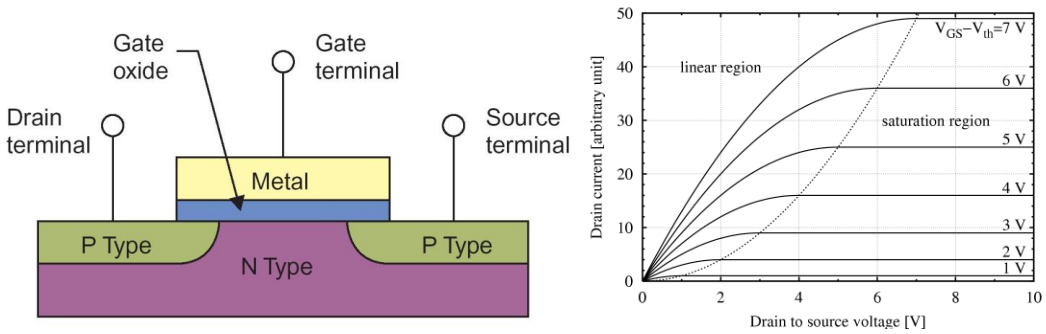

Figure 1-2 Images of Metal Oxide Semiconductor Field Effect Transistor (MOSFET) and its I-V characteristics.

Due to electrical considerations, the gate oxide thickness must be proportional to the gate length in terms of such factors as the distance between the source and drain. The lateral scaling of transistor dimensions thus directly translates into a reduction in the gate-oxide thickness. When the gate thickness is scaled to the sub-10-nm range, the exponentially increased charge leakage makes it difficult to further advance silicon

semiconductor technologies. Therefore, at this range of thickness, quantum mechanical tunneling currents through the oxide become intolerable. For more efficient information processing, innovative devices must be developed.

Information can be encoded, transported, and stored using both electron charge and spin- that latter of which is an elusive property of electrons that may just be the next entity for data encoding. The connection between electron transport and spin plays a major role in information transport through devices. Since spin is usually associated with quantum mechanics, any devices relying on it are termed *quantum devices*. When dealing with spin, it is expected that tiny length scales within the device come into play. For information to be reliably encoded and transported from one part of a spintronic device to another using the spin associated with electrons, certain conditions must be met. Current research has focused on examination of these conditions as well as the means of eliminating the challenges encountered in spin injection, transport and detection.

Regarding the advantages of spintronics, spintronic devices have the potential to be scaled to the sub-1-nm range to resolve the scaling problem encountered in current FET [5]. Moreover, spintronics promises to give birth to a new breed of computing devices with such important advantages as non-volatility, data densities above 100 terabit/in^2, data rates in the terahertz range, and negligible levels of power consumption.

However, to realize the potential of many groundbreaking applications, new materials that combine both magnetic and semiconducting properties at room temperature must be developed [6]. Since the early 1990s, extensive research has been conducted to explore the feasibility of using (III, Mn)-V diluted magnetic semiconductors (DMS) as

room-temperature ferromagnetic semiconductors [7]. Unfortunately, increasing Curie temperatures from the current record of approximately 200 K remains the main roadblock for further research into DMS materials.

Hence, the tremendous current interest in *graphene*, a substrate composed of several single layers of *graphite*, defined as a monolayer of carbon atoms densely packed in a honeycomb lattice, is not surprising. Since being first synthesized in 2004 [8, 9] through micro-mechanical cleavage and epitaxial growth, graphene has become one of the most remarkable materials in carbon-based science and engineering on the nanometer scale. It is only one atom thick but stable under ambient conditions, and exhibits extraordinarily high crystal and electronic quality. The most important properties of graphene originate from its very unusual electronic properties; in other conductors, charge carriers are described in terms of quantum mechanics as electron waves obeying the Schrödinger equation- the wave equation of quantum physics, whereas graphene electrons are described according to the laws of relativistic quantum physics obeying the Dirac equation. Recent theoretical and experimental efforts have indicated that graphene may indeed be the long-sought-after material due to relatively small spin-orbit interaction [9, 10, 11, 12].

Moreover, theory predicts an entire spectrum of magnetic phenomena in graphene, including several mechanisms for intrinsic ferromagnetism and spin-ordering effects that arise due to its low dimensionality and Dirac-like spectrum. However, none of these effects has yet been explored experimentally. If confirmed, the existence of spin ordering in graphene will have important implications for not only understanding of this

remarkable material but also for its various applications and the field of spintronics in general.

Further research into graphene will help to resolve the controversies regarding recent findings of magnetism in so-called unconventional carbon-based magnetic materials. Ferromagnetism has been detected in these materials despite the absence of atoms with partially filled d- or f- orbital that have non-zero total spin. However, the findings remain highly controversial, and there are many uncertainties related to the experimental system. Therefore, further research should seek unambiguous answers to questions related to magnetism in other graphitic materials, in which the inevitable presence of impurities and imperfections can obscure vital evidence or lead to artifacts.

1.2 **Historical Overview**

Carbon is the chemical element represented by the symbol “C” and the sixth atomic number. As an element that exists abundantly in the earth and universe, it is very important in our daily lives. In nanotechnology, it is a key element in mechanics, chemistry, physics, and electronics. Pure atomic carbon exists and is categorized by its four different crystalline forms - Diamond, Graphite, Fullerenes, and Nanotubes - each of which is characterized by properties related to hybridization, density, and bonding length, as well as electronic and mechanical properties, as shown in Table 1-1. Other common forms of carbon are amorphous carbon, charcoals, soot, and glassy carbon

(microcrystalline forms of graphite). Before C_{60} was discovered in 1985, diamond and graphite were the two well-known forms of crystalline carbon.

Table 1-1 Properties of Carbon Allotropes.

Dimension	0-D	1-D	2-D	3-D
Isomer	Fullerene	CNT	Graphene	Diamond
Hybridization	Sp2	Sp2	Sp2	Sp3
Density [g/cm^3]	1.72	1.2 – 2.0	2.26	3.52
Bond length (Å)	1.40 (C=C)	1.42 (C=C)	1.42 (C=C)	1.54 (C-C)
Electronic Properties	Semiconductor (E_g = 1.90)	Semiconductor / Metal	Semi-metal	Insulator (E_g =5.47)
Mechanical Properties	14 GPa	1 – 5 TPa	> 0.5 TPa	1050 Gpa

Since their discovery by Sumio Iijima in 1991, scientists and engineers have been researching the properties and applications of *carbon nanotubes* (CNTs), which has resulted in theories and methods for their synthesis. Recent research has recategorized

graphene, a quasi-2D monolayer of graphite, into three crystalline forms - curling, rolling, and stacking – which can turn graphene into buckyballs, nanotubes, and graphite, respectively, as shown in Figure 1-3 [13].

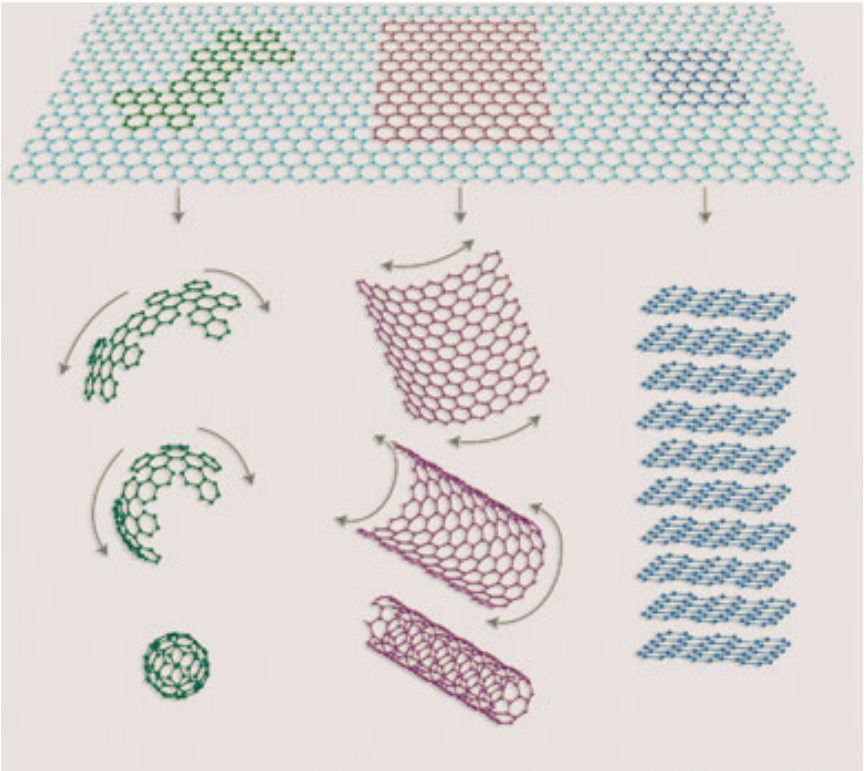

Figure 1-3 Curling, rolling, and stacking of graphene into buckyballs, nanotubes, and graphite, respectively [13]

Fullerenes have a graphite-like structure, but instead of purely hexagonal packing, which is possible with pentagons or heptagons of carbon atoms, they bend the sheet into

spheres, ellipses, or cylinders. The properties of fullerenes, which split into buckyballs, buckytubes, and nanobuds, have not yet been fully analyzed, and therefore represent an intense area of research in nanomaterials. The terms *"fullerene"* and *"buckyball"* were given in recognition of Richard Buckminster Fuller, popularizer of geodesic domes, which, as shown in Figure 1-4 [14], resemble the structure of fullerenes.

Figure 1-4 The Montreal Biosphère, formerly the US Pavilion at Expo 67, built by R. Buckminster Fuller & S. Sadao on Île Sainte-Hélène, Montreal, Canada [14]

Buckyballs are covalently bonded to the outer wall of a nanotube that combines the properties of both in a single structure. For the past decade, the chemical and physical properties of fullerenes have been intense areas of interest in the field of research and

development, and are likely to be so for many years to come. Fullerenes have been primarily studied for their potential medical applications, as binding specific antibiotics to the structure can target resistant bacteria and even certain cancer cells, such as melanomas. One study has demonstrated the effectiveness of fullerenes as light-activated antimicrobial agents [15].

In the field of nanotechnology, heat resistance and superconductivity are two of the most heavily studied properties. A common method for producing fullerenes is to send a large current between two adjacent graphite electrodes in an inert atmosphere. The resulting carbon plasma arc between the electrodes cools into a sooty residue from which many fullerenes can be isolated. Many calculations that have been made using ab-initio Quantum Methods have been applied to fullerenes. By using DFT and TD-DFT methods, infrared, Raman, UV spectra of fullerenes are characterized to be compared with experimental results.

CNTs are carbon allotropes with a cylindrical nanostructure. The term *nanotubes* is derived from the size of the structure, having a diameter of only several nanometers but being up to several millimeters in length. Categorized as single-walled nanotubes (SWNTs) and multi-walled nanotubes (MWNTs), nanotubes are members of the fullerene structural family, which also includes the spherical buckyballs. The ends of a nanotube might be capped with a hemisphere of the buckyball structure. Nanotubes have been constructed with length-to-diameter ratio of up to 28,000,000:1 [16], which is significantly larger than any other materials. These cylindrical carbon molecules have novel properties, including extraordinary strength, unique electrical properties, and

efficiency in heat conduction that make them potentially useful in many applications, especially in the fields of nanotechnology, electronics, optics and architecture. However, many of their applications are limited by their potential toxicity.

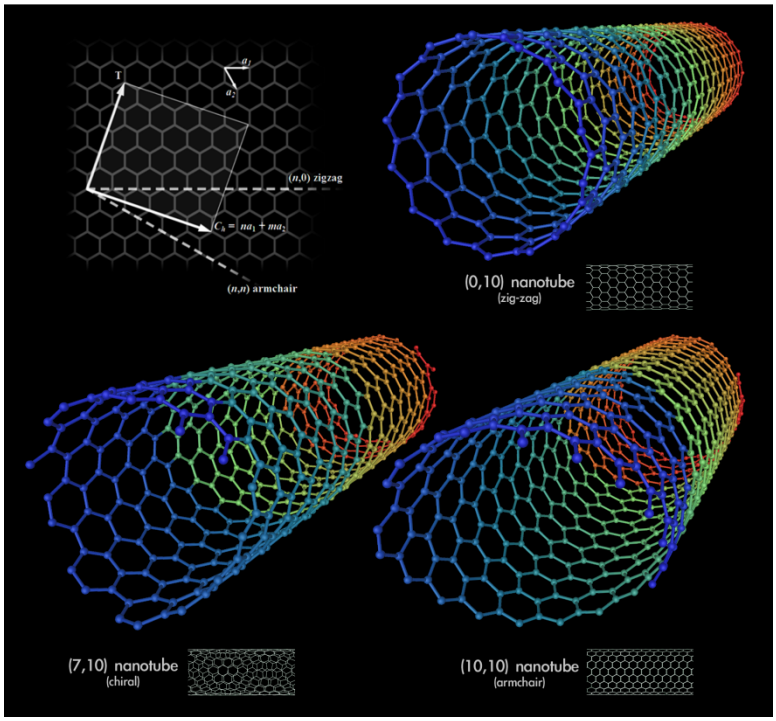

Figure 1-5 Types of Single wall Carbon nanotubes [17]

The nature of nanotube bonding is described by applied quantum chemistry, specifically orbital hybridization. The chemical bonding of nanotubes is composed entirely of sp2 bonds, similar to those of graphite. This bonding structure, which is stronger than the sp3 bonds found in diamonds, provides the molecules with their unique

strength. Nanotubes naturally align themselves into “ropes” held together by van der Waals forces. Under high pressure, nanotubes can merge, trading some sp2 bonds for sp3 bonds, and thus giving the possibility of producing strong wires of infinite length through high-pressure nanotube linking.

During first few years of this decade, few researchers expected that one-atom-thick sheets of graphene could experimentally exist in a freestanding state. Conventional wisdom based on decades-old thermodynamics arguments held that “freestanding” graphene, meaning a one-atom-thick film that is somehow suspended or resting on a nonbinding support such as silicon dioxide, would be unable to resist the “urge” to roll into a nanotube or other curved structure. Starting with flecks of graphite generated by mechanical cleavage, these small specks of carbon onto adhesive tape folded the sticky sides against the tiny crystals, cleaving the flakes in two when the tape is pulled apart. By repeating this rather rudimentary splitting process several times, thinner and thinner slices are generated that are stable at room temperature; indeed, one-atomic thick bits of graphene remain surprisingly stable even at room temperature.

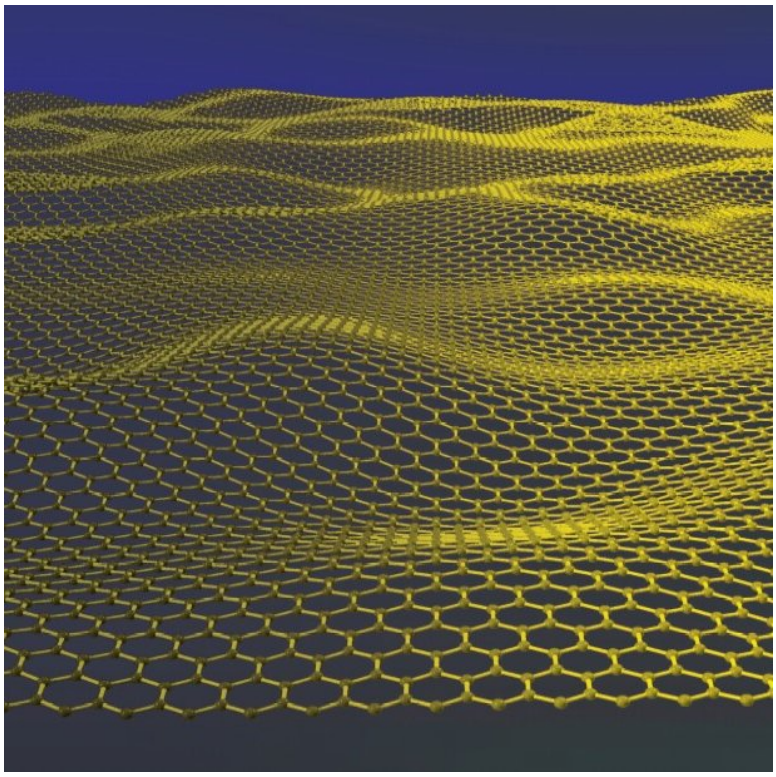

Figure 1-6 Wavy Form of Graphene [18]

After the 2002 discovery of a type of pure carbon that is magnetic at room temperature, the conventional knowledge regarding magnetic materials has been subject to controversy. Since then, theoretical research has predicted an entire spectrum of magnetic phenomena in graphene, including several mechanisms for intrinsic ferromagnetism and spin-ordering effects that arise due to its low dimensionality and Dirac-like spectrum. However, none of these effects has yet been explored experimentally. Nevertheless, ferromagnetism of graphene itself and chemically modified

graphene was recently indentified indicating that epitaxial graphene with functionalization form may make a role of magnetic semiconductor.

The existence of spin ordering in graphene has important implications for not only understanding this remarkable material with its chemical functionalization form, but also for its various applications, including in magnetic semiconductors and in spintronic devices for information processing and data storage. Using unconventional materials such as fullerenes, bulk graphite, and graphene, ferromagnetism has been detected in spite of the absence of atoms that have non-zero total spin. However, such findings remain highly controversial, as there are many uncertainties related to the experimental system with and/or without any crystal defects and impurities in the lattice of graphene. Therefore, clear answers are needed to to questions related to magnetism in other graphitic materials, in which the inevitable presence of impurities and imperfections can obscure vital evidence or lead to artifacts.

When considered together, the spin and the charge of the electron offer many opportunities for the creation of new information processing and storage devices [5]. However, in order for spintronics to achieve its promise, a material that combines both magnetic and semiconducting properties at room temperature is required. When randomly functionalized with aryl radicals, graphene functions as a room temperature ferromagnet, which suggests that such functionalized graphene may form the basis for a new approach to magnetic semiconductors. This finding suggests that such functionalized graphenes may form the basis for a new approach to magnetic semiconductors.

1.3 **Summary**

This study conducted research into the electronics and magnetism of two types of nano-carbon: epitaxial grown multilayered graphene and functionalized graphene with aryl radicals. This research focused on demonstrating that functionalized graphene with aryl radicals behaves as a room temperature ferromagnet, a phenomenon that, together with the observation of transport studies, suggests the basis of a new approach to magnetic semiconductors.

Chapter 1 provides an overview of silicon-based semiconductor technology, describes its current limitations, and discusses the unique properties of alternative carbon-based material technologies, including graphene-based electronics and magnetism for spintronic devices and other carbon allotropes.

Chapter 2 reviews major fabrication approaches for graphene that have been used to date in a variety of ways. The chemical functionalization of epitaxial graphene is described.

Chapter 3 discusses the electronics of graphene, focusing on transport study of temperature dependence and magnetoresistance that demonstrated the characteristics of graphene with chemical functionality throughout the temperature range from 2K to 300K.

Chapter 4 describes the magnetism of graphene by the reference to research into M-H hysteresis loops, magnetic force miscroscopy, magneto-optical Kerr effect microscopy, MFM tip fabrication, and sample mounting methods.

Chapter 5 provides the study conclusions by discussing the possibility of producing a pure 2D magnet with superior anisotropy based on current findings. It recommends directions for future research in the areas of graphene-based magnetism and magnetic semiconducting devices.

2. Fabrication Methods

2.1 Introduction

For centuries, graphite has been widely and commonly used as the main component of pencils. Every time someone scribes a line with their pencil, the resulting mark contains some layers of graphene. However, graphene has rarely been produced in its freestanding single-sheet form in order to explore and exploit its many properties. Scientists have been trying to split graphite into its constituent parts for many years, and after extensive researches have been developed, four different fabrication methods of graphene are so far reported: chemical vapor deposition [19], micromechanical exfoliation [20], chemical exfoliation [21], and epitaxial growth of graphene [8].

After being used for decades, CVD has recently gained much attention due to its wafer size growth with high quality. Micromechanical exfoliation of graphite, also known as the “Scotch tape” or “peel-off” method, was developed from earlier work on micromechanical exfoliation from patterned graphite, and is currently the most popular means of synthesis. Chemical exfoliation of graphite, which was first developed in the nineteenth century to exfoliate graphene, is now used to create colloidal suspensions [21]. The epitaxial growth of graphene is the growing of graphene on the insulating substrate, silicon carbide [8]. Since 2004, micromechanical exfoliation and the epitaxial growth of graphene have been used for synthesizing single crystal of graphene lattice.

2.2 Growth of Graphene on SiC

An epitaxially grown graphene monolayer is formed from the segregation of carbon in silicon carbide substrates. Observation of segregation has provided evidence of a surface - phase transition due to not only the strong carbon-carbon interactions within a graphite monolayer but also a good epitaxial fit to the substrate. Currently, most graphene samples are prepared by stripping off layers of graphite, which consists of multiple layers of graphene and is the ground state of carbon.

To produce the epitaxial growth of graphene, large areas of graphene are prepared by evaporating silicon from silicon carbide. As the silicon evaporates, it leaves behind sheets of graphene, with the number of graphene layers depending on the evaporation temperature and time. This ability to prepare large areas of high-quality graphene on a substrate is a necessary step by offering the only means of using graphene in electronic applications.

Epitaxial graphite films are produced on the C- and Si-terminated faces of single-crystal 6H-SiC or 4H-SiC by thermal desorption of Si [8]. After surface preparation by oxidation or H_2 etching, samples are heated by electron bombardment in ultrahigh vacuum in order to remove the oxide, with some samples being oxidized/deoxidized several times to improve the surface quality. Atomic force microscopy images have indicated that the best initial surface quality is obtained with H_2 etching. By heating to high temperatures in furnace, thin graphite layers are formed of thickness determined predominantly by the temperature.

Of the several graphene layers of which epitaxial graphene is composed, only the first layer is electron doped due to the built-in electric field, with the other layers being essentially undoped. The charge carriers show Dirac particle properties, such as an anomalous Berry's phase, weak anti-localization, and square root field dependence of the Landau level energies [22]. They also show quasi-ballistic transport and long coherence lengths, properties that may persist above cryogenic temperatures [23]. These favorable features indicate that interconnected room-temperature ballistic devices may be feasible for low-dissipation high-speed nanoelectronics [24].

2.3 **Micro-Mechanical Exfoliation**

Mechanical exfoliation of graphite became the first identified synthesis method when it was initially performed in 2004. In the absence of quality graphene, most researchers use samples obtained by micromechanical cleavage of bulk graphite, the same technique that allowed for the initial isolation of graphene [8, 20]. After fine-tuning, this technique can provide high-quality graphene crystallites up to 100 µm in size, which is sufficient for most research purposes.

By rubbing or scraping graphite against a surface, microscopic chunks as thin as roughly 100 atomic layers could be peeled off the substrate. More recently, researchers attached a graphite crystal to an atomic force microscope (AFM) tip and used the device to make nanometer-sized graphite markings on silicon wafers. With this AFM "writing"

instrument, fondly referred to as the “nanopencil,” they could decorate wafers with around 10 to 20 layers of very thin graphite crystallites.

The micromechanical cleavage technique highlights several features of 2D crystals that may explain why 2D crystals were not discovered earlier. First, monolayers accompany a great number of thicker flakes. Second, unlike nanotubes, 2D crystals have no clear signatures in transmission electron microscopy. Third, because monolayers are completely transparent to visible light, they cannot be seen on most substrates, including glass and metals, when using an optical microscope. Fourth, the AFM method is currently the only method that allows definitive identification of single-layer crystals, but it has a very low throughput (especially when high-resolution imaging is required), and in practice it would be impossible to find cleaved 2D crystallites by scanning surfaces at random. Finally, it is not certain that isolated atomic planes could survive without their parent crystals. Micromechanical cleavage of bulk graphite provides an approach to obtaining isolated graphene monolayers that appears no more complicated than repeatedly applying a piece of adhesive tape to graphite until the thinnest flakes can be peeled off the substrate. To date, high-quality graphene crystallites up to 100 μm in size have been synthesized using the micromechanical cleavage method. The synthesis of isolated graphene monolayers greatly promotes the investigation of the unique properties and potential applications of graphene.

The main procedure for the micromechanical cleavage of bulk graphite begins by obtaining the starting material of 1-mm-thick platelets of highly-oriented pyrolytic graphite (HOPG). Scotch tape is then repeatedly applied to peel off flakes of graphite

with the thin flakes left in the tape. Then, the thin flakes in the tape are gently pressed onto a Si wafer to transfer to several flakes on the wafer's surface. Ultrasound cleaning in propanol is then conducted to remove mostly thick – flakes, as thin flakes (d<10nm) have been found to attach strongly to SiO_2, presumably due to van der Waals and/or capillary forces.

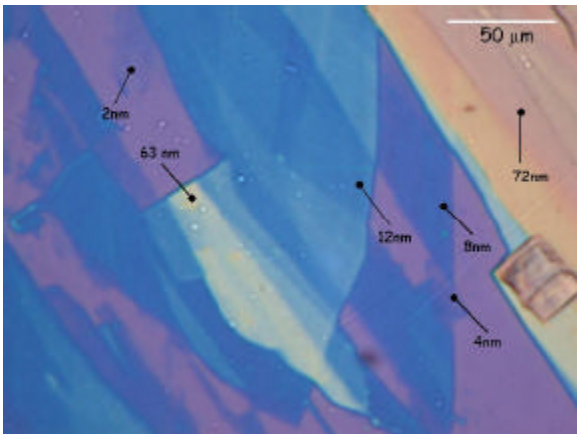

Figure 2-1 Optical Microscopy of Graphene: white light of graphitic films of various thickness ~d. The indicated values of thickness were measured by Atomic Force Microscopy [9].

A combination of optical, electron-beam, and atomic-force microscopy can be used to select from among the resulting films those that are only a few graphene layers thick. Graphitic films thinner than 50nm are transparent to visible light yet can easily be seen on the SiO_2 surface because of the added optical path that shifts the interference colors.

The color of a 300-nm wafer is violet-blue, with the extra thickness due to graphitic films shifting the color to blue as shown in Figure 2-1 [9].

2.4 Chemical Oxidation and Exfoliation of Graphite

Early researchers of the chemical exfoliation of graphite attempted to insert molecules or atoms between the layers of graphite to exfoliate the graphene sheets. This chemical exfoliation technique generally yielded a slurry or sludge of graphitic particles similar to wet soot such that the graphene layers were rolled up to decrease the surface energy. Although it was difficult to detect single layers of graphene in the compounds resulting from the chemical exfoliation of graphite, this method soon led to the development of the mechanical approach to cleaving graphite.

Graphite oxide has been mainly produced by the Hummer [25] and other methods [26, 27] since it was first prepared in the nineteenth century. All methods involve oxidation of graphite as bi-products of strong acids and oxidants treatment. The level of the oxidation depends on experimental factors, such as the reaction conditions and the precursor graphite used. Although extensive research attempted to identify the chemical structure of graphite oxide, no single method of doing so has been developed, with the several models developed thus far remaining subject to debate. In later years, graphite films of several single layers were synthesized by a chemical exfoliation method using graphite intercalates compounds [28]. Eventually, the total exfoliation of graphite was

achieved from the polymerization of unsaturated hydrocarbon conducted in the inter-spacing of graphite using potassium as the initiator or catalyst [21].

To date, several methods have been developed for the chemical exfoliation of graphene, which basically, involves the oxidation of graphite with strong acids and oxidants. The level of the oxidation, which is the bi-product of oxidation, depends on the method applied, the reaction conditions, the graphite used, and several other factors [21]. Although extensive research has revealed the basic chemical structure of graphite oxide, which is shown in Figure 2-2 [29], the exact chemical structure of graphene oxide remains unclear.

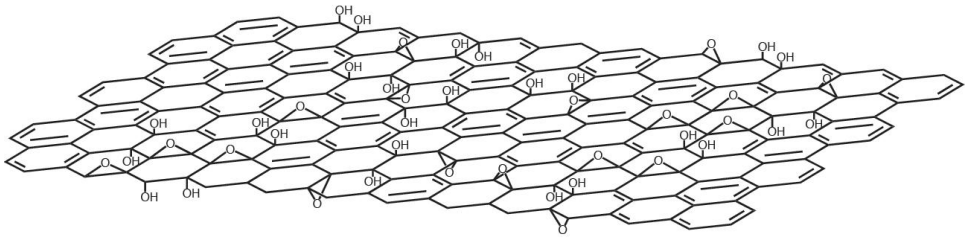

Figure 2-2 Chemical structure of graphite oxide [29].

The sp2-bonded carbon network of graphite is strongly disrupted, and a significant fraction of this carbon network is bonded to hydroxyl groups or participates in epoxide groups [29, 30, 31, 32]. Graphite oxide thus consists of a layered structure of “graphene oxide” sheets that are so strongly hydrophilic that the intercalation of water molecules

between the layers readily occurs [33]. The interlayer distance between the graphene oxide sheets increases reversibly from 6 to 12 Å with increasing relative humidity [33]. Notably, graphite oxide can be completely exfoliated to produce aqueous colloidal suspensions of graphene oxide sheets by simple sonication [34] and by stirring the water/graphite oxide mixture for a sufficient length of time [35].

Considerable research into such aqueous colloidal suspensions was performed in the 1950s and 1960s [36, 37]. Because graphene oxide sheets most likely have a chemical structure similar to the layers in graphite oxide, they are a promising starting material for the generation of colloidal suspensions of other chemically modified forms of graphene through chemical tuning [21]. Filtration of chemically modified graphene suspensions has produced free standing paper-like materials [38, 39, 40, 41, 42] that have a layered structure. Significant advances have also been made in using homogeneous suspensions of chemically modified graphene sheets to produce thin films, which can be relevant to transparent and electrically conductive thin-film applications, among others [43, 44, 45].

2.5 Chemical Vapor Deposition

One of the ground breaking approaches for the high-quality wafer level fabrication of graphene is the CVD approach [19, 46], in which carbon is dissolved into the nickel substrate. As shown in Figure 2-3, the CVD method requires dissolving carbon onto thin metallic film, cooling the substrate, to produce carbonaceous gas, and then precipitating the gas out of the substrate. The resulting thickness and crystalline ordering of the

precipitated carbon depends on the cooling rate and the concentration of carbon dissolved in the substrate. This concentration is in turn controlled by the type and concentration of the carbonaceous gas and the thickness of the metallic layer. After a chemical etching with the nickel etchant, the graphene membrane detaches, and can be transferred to another substrate. This direct CVD synthesis provides high-quality layers of graphene without the need for intensive mechanical or chemical treatment. Using this method, graphene samples of several square centimeters and excellent electrical and optical properties have been fabricated.

The thickness and crystal structure of the carbon depends on the cooling rate and the concentration of the carbon dissolved into the nickel, as carbon precipitates out by cooling nickel. This concentration in turn depends on the type and concentration of the carbonaceous gas and the thickness of the nickel layer. After a chemical etching of the nickel, the graphene membrane detaches and can be transferred to another substrate. This direct CVD synthesis provides high quality layers of graphene without the need for intensive mechanical or chemical treatment.

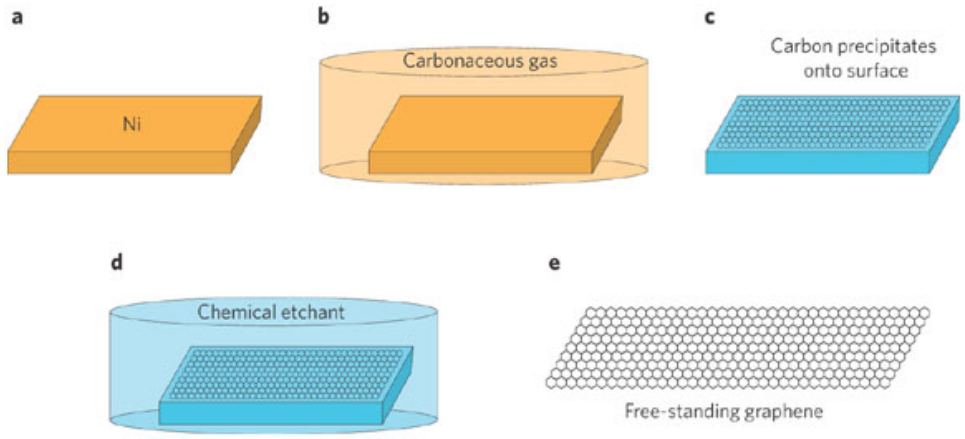

Figure 2-3 a) A thin layer of nickel (Ni) is deposited onto a substrate; The crystallinity of this layer depends on its thickness, annealing, and the nature of the substrate. b) The Ni layer is heated to about 1,000 °C and exposed to a carbonaceous gas environment. Carbon atoms are generated at the Ni surface and diffuse into the metal. c) As the nickel is cooled, the carbon atoms precipitate out of the nickel layer and form graphene on its surface. The graphene samples are expected to form on the (111) faces of Ni crystallites. d) The graphene membrane is detached from the Ni layer by gentle chemical etching. e) The resulting free-standing graphene layer is transferred onto appropriate substrates. Colors illustrate the difference in temperature (orange color represents hot; blue shows cold) and chemical composition (orange shows gas; blue represents etchant) [47].

The graphene films produced by CVD demonstrate excellent electronic [19] and optical properties [19, 46], including a sheet resistance as low as 280 cm^{-2}, a carrier

mobility as high as 3,700 cm^2/Vs, and a 90% optical transparency, although these values are inferior to those obtained for a perfect single layer of graphene [20]. Researchers have reported that graphene films produced by CVD are useful for producing flexible and transparent electrodes for solar cells and liquid crystal displays, as well as for producing various electronic and optoelectronic devices with high frequency. The combination of its low cost, scalability, and advanced material properties make the CVD approach exceptional.

Even though the further development of the large-scale CVD deposition of graphene for industrial purposes will largely depend on engineering research, fundamental research also has a role to play. Replacing the polycrystalline substrates with the single-crystal nickel substrates used to grow epitaxial graphene would reduce the number of defects in the samples by reducing the mismatch between the nickel and graphene lattices. A significant obstacle to CVD technology is that the large difference in the thermal expansion coefficients of nickel and graphite leads to ripple structures in the samples. This obstacle must overcome to achieve the planar graphene film topology required for the micro-patterning of electronic devices.

The successful production of large-area graphene from CVD is a promising step towards the industrial production of graphene-based electronic and optoelectronic devices. The use of large-scale CVD graphene as a flexible and optically transparent electrical contact has been demonstrated [19, 46, 47]. Such flexibility and transparency lead this form of graphene to provide significant advantages in terms of carrier mobility and mechanical strength and flexibility over conventional metal oxides in the production

of liquid crystal devices, solar cells, and organic light-emission devices, as well as quantum coherent devices in which phase coherent electron transport is used for new device functionalities or improved performance. The scalability of CVD graphene technology may hasten the transition from the production of single electronic devices to the production of complex integrated circuits containing numerous active and passive graphene-based components [47].

2.6 **Chemical Functionalization of Graphene**

For the large scale production of electronic devices at the molecular level, the processing steps, which are essential for the development of highly integrated graphene electronics, require the realm of organic chemistry instead of physical engineering of graphene using traditional lithographic processes. The chemical formation of carbon−carbon bonds offers an alternative approach to the control of the electronic and magnetic properties of epitaxial graphene [48, 49, 50].

The transformation of the carbon centers from sp2 to sp3 introduces a barrier to electron flow by opening a band gap and allows the generation of insulating and semiconducting regions in graphene wafers [48, 49]. Moreover, the addition of an aryl radical is the generation of a delocalized π-radical and detailed calculations and experimental results show that spin density is delocalized over many carbon atoms with the highest spin density in the vicinity of the point of attachment of the aryl group [50, 51].

The epitaxial graphene (EG) samples as described in Section 2.3 are thermally grown in vacuum on the [0001] face of diced SiC wafers (dimension 3.5 mm × 4.5 mm) after surface flattening by hydrogen etching. The EG is characterized by surface analysis tools such as X-ray and low-energy electron diffraction methods in ultra-high vacuum by indicating the presence of 5-10 layers of epitaxial graphene on the (0001) face with a structural coherence greater than 300 nm [8, 22, 23].

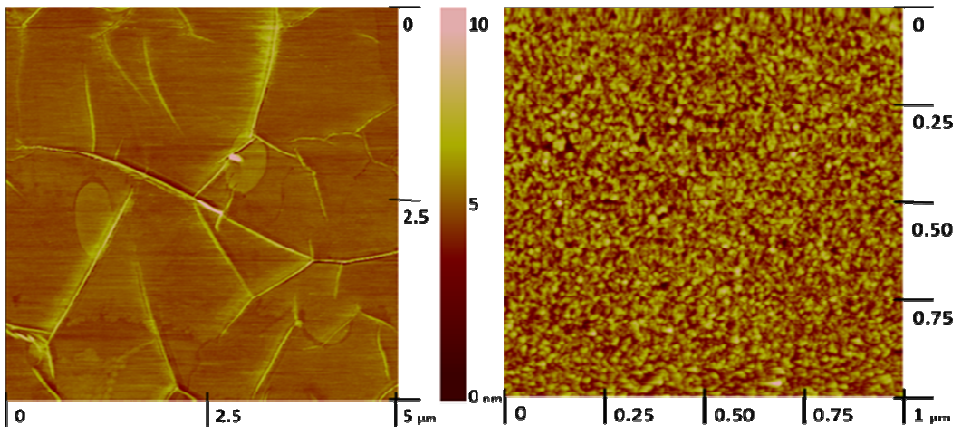

Figure 2-4 AFM images of: (L) pristine epitaxial graphene (EG), (R) nitrophenyl functionalized epitaxial graphene (NP-EG).

Then, EG substrates are chemically functionalized with nitrophenyl groups by spontaneous electron transfer to the corresponding diazonium salt [48]. This solution-based, room temperature chemical functionalization procedure is exceedingly gentle and leads to the covalent attachment of the aryl groups to the basal plane carbon atoms in the

top graphene layer [50]. The detailed AFM images of EG samples are shown in Figure 2-4 before and after functionalization.

3. Transport Properties of Graphene

3.1 Transport Study

The resistivity ρ, which is an intrinsic property of materials, is important for starting material as well as for semiconductor devices for electronics. Although carefully controlled during crystal growth, it is not truly uniform in the grown process due to variability during growth and segregation coefficients less than unity for the common dopant atoms. The resistivity of silicon wafers is usually modified locally during device processing by diffusion, ion implantation, and other factors.

The resistivity depends on the free electron and hole densities, n and p, and the mobility of electron and hole, μ_n and μ_p, respectively, according to the relationship as follows:

$$\rho = \frac{1}{e\left(n\mu_n + p\mu_p\right)} \tag{3.1}$$

For extrinsic materials in which the majority carrier density is much higher than the minority carrier density, it is generally sufficient to know the majority carrier density and the majority carrier mobility. However, the carrier densities and mobility are generally not known. Hence, alternative measurement techniques, ranging from contactless, through temporary contact to permanent contact techniques need to be introduced.

The four-point probe is commonly used for the measurement of the resistivity of the materials. It is an absolute measurement without recourse to calibrated standards and is sometimes used to provide standards for other resistivity measurements. Since only tow probes are needed for the manipulation, two-point probe methods would appear to be easier to implement. However, the interpretation of the measured data is more difficult as shown in Figure 3-1. By using four probes rather than two, the voltage is measured with two additional contacts between two contacts for current and so parasitic voltage drops could be eliminated.

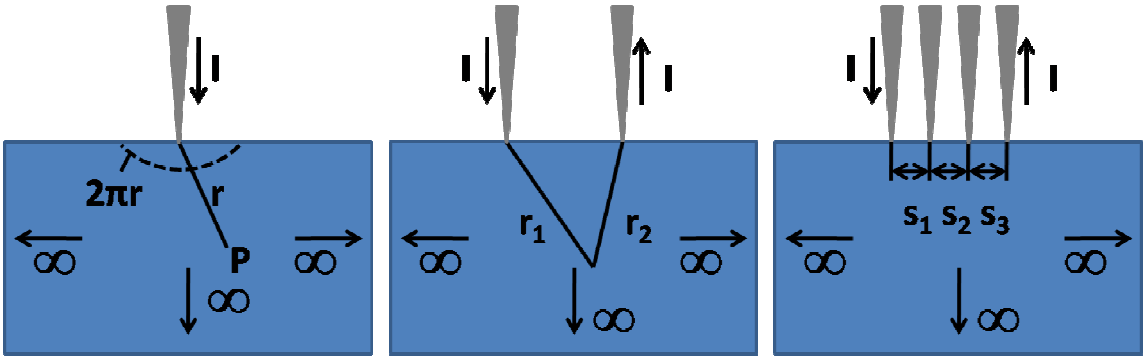

Figure 3-1 Schematics of one-, two-, and four-Point Probes Measurement.

The four-point probe was firstly proposed by Wenner [52] to measure the earth's resistivity in 1912. To derive the four-point probe resistivity expression, by starting the sample geometry in Figure 3-1 [53], the electric field ε is related to the current density J, the resistivity ρ, and the voltage V as follows:

$$\varepsilon = J\rho = -\frac{dV}{dr}; J = \frac{I}{2\pi r^2} \tag{3.2}$$

The voltage at point *P* at a distance *r* from the probe is then expressed as:

$$\int_0^V dV = -\frac{I\rho}{2\pi}\int_0^r \frac{dr}{r^2} \Rightarrow \frac{I\rho}{2\pi r} \tag{3.3}$$

For the configuration in Figure 3-1, the voltage is as follows:

$$V = \frac{I\rho}{2\pi r_1} - \frac{I\rho}{2\pi r_2} = \frac{I\rho}{2\pi}\left(\frac{1}{r_1} - \frac{1}{r_2}\right) \tag{3.4}$$

where r_1 and r_2 are the distance from probes 1 and 2, respectively.

The minus sign accounts for current leaving through probe 2. For probe spacings s_1, s_2, and s_3, as in Figure 3-1, the voltage at probe 2 is expressed as:

$$V_2 = \frac{I\rho}{2\pi}\left(\frac{1}{s_1} - \frac{1}{s_2 + s_3}\right) \tag{3.5}$$

and at the 3rd probe, the voltage is expressed as follows:

$$V_3 = \frac{I\rho}{2\pi}\left(\frac{1}{s_1+s_2} - \frac{1}{s_3}\right) \tag{3.6}$$

The total measured voltage $V = V_{23} = V_2 - V_3$ becomes as the follow expression:

$$V = \frac{I\rho}{2\pi}\left(\frac{1}{s_1} - \frac{1}{s_2+s_3} - \frac{1}{s_1+s_2} + \frac{1}{s_3}\right) \tag{3.7}$$

The resistivity ρ is given:

$$\rho = \frac{2\pi}{\left(1/s_1 - 1/(s_1+s_2) - 1/(s_1+s_2) + 1/s_3\right)}\frac{V}{I} \tag{3.8}$$

The current is usually such that the resulting voltage is approximately 10 mV. For most four-point probes, the spacings between the probes are equal and so $s = s_1 = s_2 = s_3$, equation 3.9 reduces to:

$$\rho = 2\pi s \frac{V}{I} \tag{3.9}$$

Most substrates for electronics are not semi-infinite in extent in either the lateral or the vertical dimension and equation 3.10 must be corrected for finite geometries. For an arbitrarily shaped sample the resistivity is as follows:

$$\rho = 2\pi s F \frac{V}{I} \tag{3.10}$$

where F corrects for probe location for sample thickness, sample diameter, probe placement, and sample temperature.

It is usually a product of several independent correction factors. For samples thicker than the probe spacing, the simple, independent correction factors contained in F of equation (3.10) are no longer adequate due to interactions between thickness and edge effects. Fortunately, the samples are generally thinner than the probe spacing, and the correction factors could be independently calculated in each specific case.

The sheet resistance of a material is commonly used to characterize ion implanted and diffused layers, metal films, and so on. For the two dimensional graphene layers, it is also useful to apply sheet resistance. The depth variation of the dopant atoms need not be known, as is evident from equation(3.12). The sheet resistance can be thought of as the

depth integral of the dopant atom density in the sample regardless of its vertical spatial doping density variation.

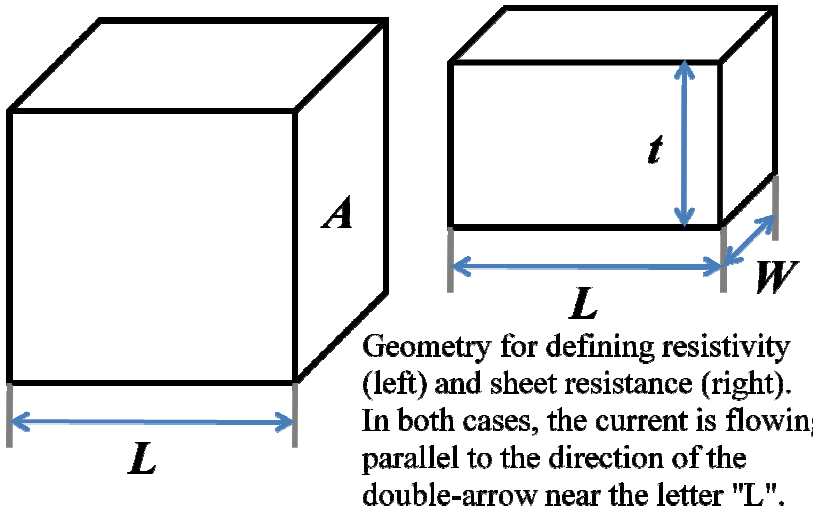

Figure 3-2 Geometries of Resistivity and Sheet Resistance. The Current is flowing parallel to the direction of the length.

To understand the concept of sheet resistance, the geometry could be considered as shown in Figure 3-2. The resistance between the two ends is given as follows:

$$R = \rho \frac{L}{A} = \rho \frac{L}{Wt} = \frac{\rho}{t} \frac{L}{W} \tag{3.11}$$

Since L/W has no units, ρ/t should have units of ohms. However, ρ/t is not the same resistance. The main idea starts from distinguishing between R and ρ/t, the ratio ρ/t is given the units of $ohms/\square$ and is named as sheet resistance, R_{sh}. Hence, the sample resistance can be written as follows:

$$R = R_{sh} \frac{L}{W} \tag{3.12}$$

Because the bulk resistance is multiplied by a dimensionless quantity (L/W) to get sheet resistance, the units of sheet resistance are ohms. However, common unit is $ohm/\square$, which is dimensionally equal to an ohm, but is exclusively used for sheet resistance. For the thin layers of graphene and/or other thin film materials, this is a great advantage of sheet resistance because a sheet resistance of a value of 1 ohm could be taken out of context and misinterpreted as a bulk resistance of 1 ohm while a sheet resistance of 1 $ohm/\square$ cannot be misinterpreted. The reason for the name "ohms per square" is that a square sheet with sheet resistance 1 ohm/square has an actual resistance of 1 ohm regardless of the size of the square. The unit could be thought of as "ohms per aspect ratio."

Because of the advantages of four-point measurement set-up, transport study of graphene was conducted by the resistivity option for the Physical Property Measurement

System (PPMS) to characterize electronic properties under cryogenic temperature from 2K to 300K and magnetic fields up to 9T. It adds a configurable resistance bridge board, called the user bridge board, to the Model 6000 PPMS Controller. None of the four channels on the user bridge board are dedicated to a specific system operation so that all four channels are available to perform four probe resistance measurements on the PPMS.

The resistivity option reports resistance and conductance as well as resistivity and conductivity. Samples for four probe measurements may be mounted on Resistivity sample pucks and/or rotation sample pucks. The rotation sample pucks are for the horizontal rotator which was used for the anisotropy measurement from out-of-plane component to in-plane component by changing the angles between magnetic field and the sample. Resistivity sample pucks have four contacts: one positive and one negative contact for current and voltage which a sample may be conventionally wired as shown in Figure 3-3.

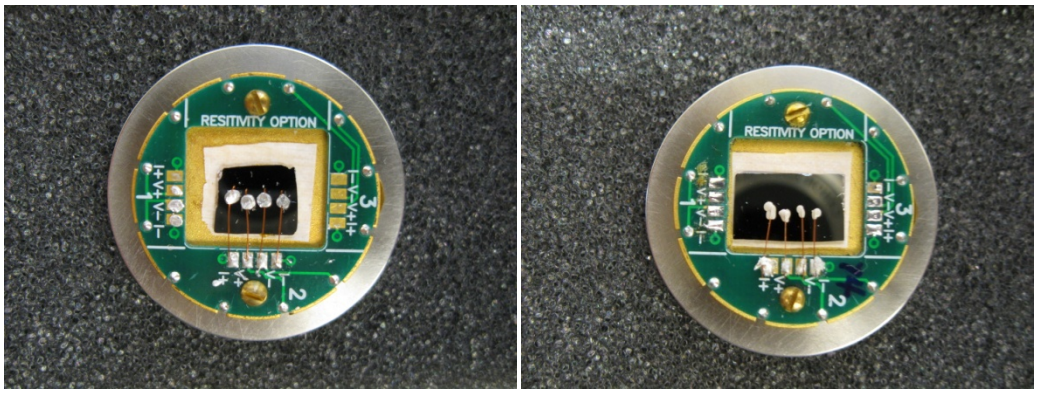

Figure 3-3 Schematics of mounting resistivity sample puck with wiring examples used in the experiments; soldering was performed outside of the sample, and then, indium contacts and conductive silver paste were applied onto samples: (a) indium contacts were used and (b) conductive silver adhesive paste was applied.

Wiring on contacts is critical issue for developing the transport measurement systems of graphene. There are popularly used methods for wiring on contacts: indium contacts, conductive silver pastes, and wire bonder. All the techniques build stable contacts under the experiment conditions. Figure 3-3 shows wiring on contacts such as indium contacts on the left and silver conductive adhesive paste on the right. To prevent the damage of sample and gold in-line contacts which deposited onto the sample, conductive silver paste is better candidate to prevent mechanical force applied when bonded.

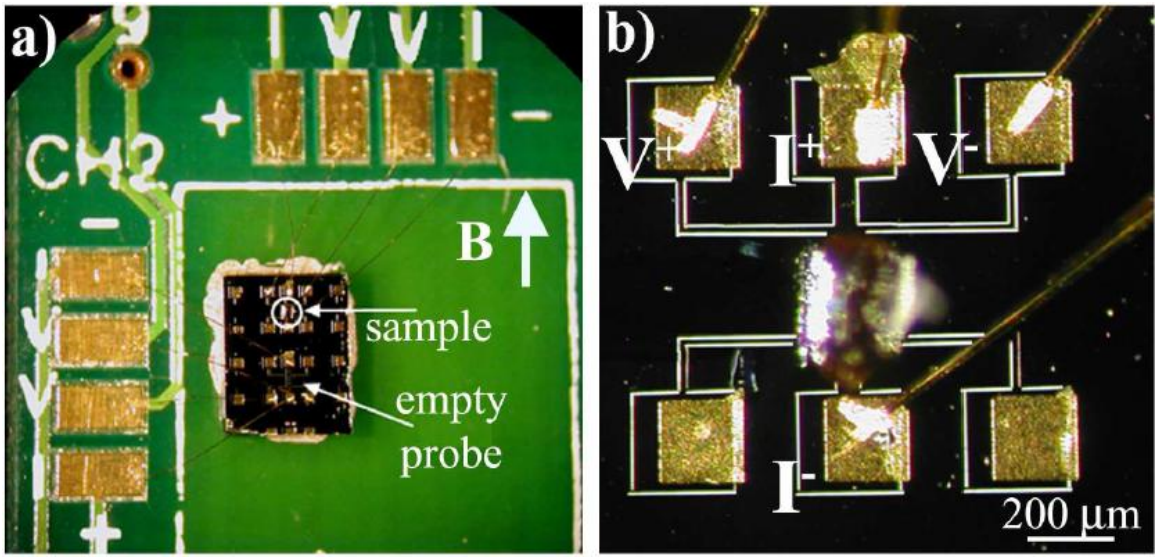

Figure 3-4 Whole view (a) & micro-view (b) of wiring contacts for Hall measurements with wire bonder; it shows uniform current flow and stable state through the measurements, but the drawback is to introduce thermal and mechanical effects from its needles when it is bonded.

As shown in Figure 3-4 [54], wiring on contacts using wire bonder introduce stable contacts for measurement systems to create uniform current flow with metallic contacts such as gold and other conductive materials. However, for the graphene project, when it is bonding, thermal and mechanical effects from needles could be applied directly through the sample to change the properties of the substrate significantly.

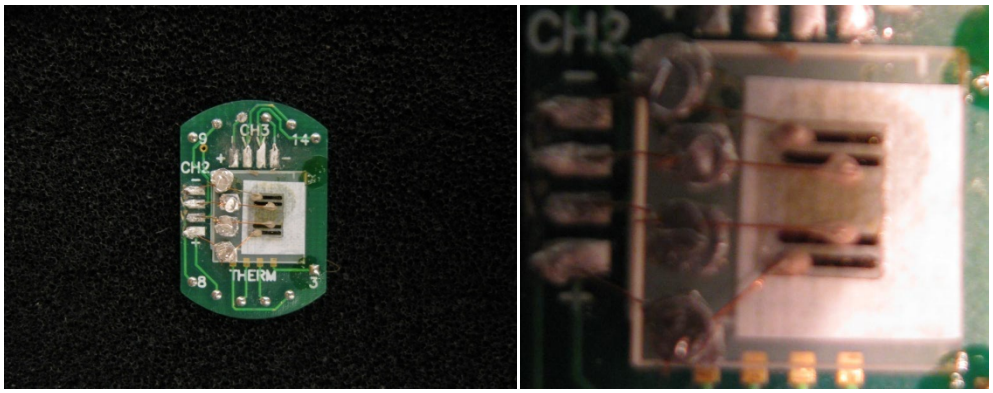

Figure 3-5 Wiring for epitaxial graphene sample; four-contacts were deposited with electron beam evaporator (100 nm of gold and 20 nm of palladium). Then, contacts were wired with silver conductive adhesive paste (from Alfa Aesar) between contacts onto EG. On user bridge contacts, indium wire (1 mm diameter and 99.999%) was applied to introduce stable contacts. Under the EG sample, cigarette paper was used to insulate electrically between the sample and board.

In order to perform the four-point resistance measurements, four in-line gold contacts (3 nm Pd, 100 nm Au) were deposited by an electron beam evaporator (Temescal BJD 1800 System) on the C-face of an EG substrate at room temperature as shown in Figure 3-5. Then, the samples were wired with silver conductive adhesive paste (from Alfa Aesar). Between contacts onto EG and user bridge contacts, Indium wire (1 mm diameter and 99.999%) was applied to ensure stable contacts. Under the EG sample, cigarette paper was used to insulate electrically between the sample and user bridge board.

Table 3-1 Resolution & Limits

Parameter	Values
Current Limit	± 0.01 – 5000 µA
Power Limit	0.001 – 1000 µW
Voltage Limit	1 – 95 mV

The user bridge board automatically adjusts the excitation current of its active channels to specify the maximum allowable current, power, and voltage for the measurement as described in Table 3-1. For the whole measurements of transport phenomena of graphene, values of 10 µA as current limit, 100 µW as power limit, and 10 mV as voltage limit were conducted for the highest resolution of the transport measurements after the optimization process.

3.2 Temperature Dependent Transport

The electronic transport properties of graphene are from the mechanism causing the scattering of its charge carriers. Scattering may result from extrinsic sources such as as charged impurities on top of graphene or in the underlying substrate [55, 56, 57], corrugation of the graphene sheet [58], phonons in graphene [59, 60, 61, 62], or remote

interfacial phonons in the substrate [62] although scanning probe microscopy studies show little evidence of intrinsic structural defects in the lattice of graphene [63, 64]. The formation of electron and hole puddles can further contribute to scattering at low carrier density [65, 66]. At low temperatures, near-ballistic transport is dominant [11]. When the temperature is increased, the resistivity exhibits two distinct behaviors, depending on carrier density: metallic and semiconducting behavior [11, 67].

The chemical functionality offers an alternative approach to the control of the electronic properties of graphene; metallic, semiconducting, and insulating depending on the coverage of the sample [48, 49]. The temperature dependence of the sample resistance was measured in the range from 2 to 300 K. Resistance versus temperature dependencies are shown for the two graphene phases under study, pristine and functionalized, respectively. As shown in Figure 3-6, while “pristine” graphene shows a change from semiconductor-like to metal-like behavior at temperature of approximately 150K, the functionalized sample acts like a “semiconductor” in the entire temperature range. It can be seen that the functionalization of graphene results in a more pronounced semiconductor-like behavior over the entire temperature range.

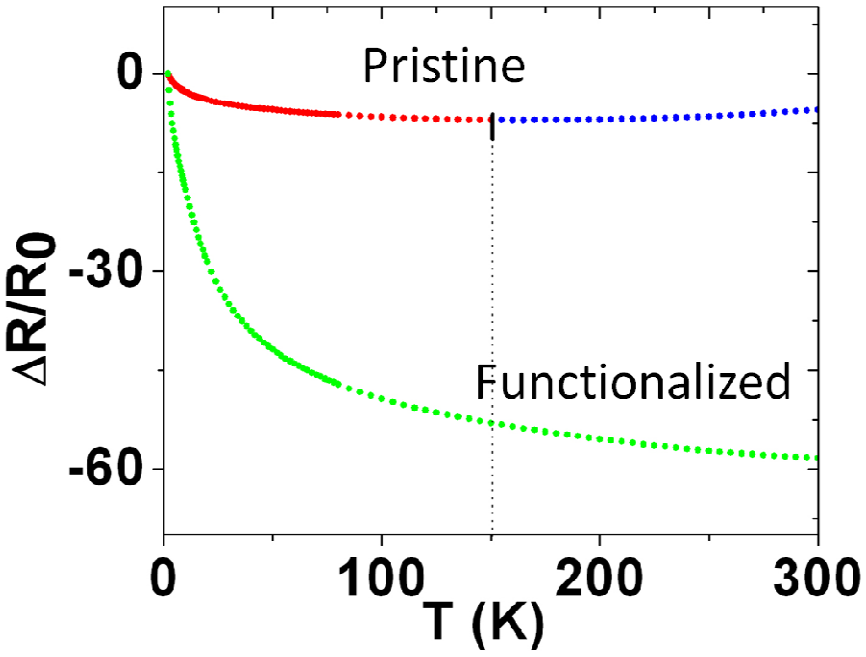

Figure 3-6 Resistance versus temperature for the pristine and functionalized stages of graphene; the values of R_0 = R (T = 2 K) are approximately 231 and 7432 Ohm for the pristine and functionalized stages, respectively.

3.3 **Magnetoresistance (MR)**

The magnetoresistance (MR) effect is a change in the electrical resistance of a substance when it is subjected to a magnetic field. The value represents as ΔR/R, which is extremely small for most substances, even at high fields, but is relative large (a few percent) for a strongly magnetic substances. The resistance of nickel increases about 2 percent and that of iron about 0.3 percent when it passes from the demagnetized to the saturated state. The effect was first discovered by William Thomson (later aka Lord

Kelvin) in 1856 [68], called ordinary magnetoresistance (OMR). More recent researches discovered materials showing giant magnetoresistance (GMR) [69], colossal magnetoresistance (CMR) [70], magnetic tunnel effect (TMR) [71], and others.

The MR of graphene investigate the fact that the chemical functionality such as the transformation of the carbon centers from sp2 to sp3 introduces magnetism with the MR and a barrier to electron flow by opening a band gap with the coverage of functionality onto the surface of graphene. Two distinct and superimposed MR mechanisms, further referred to as negative and positive MR, respectively, are shown in graphene samples.

Each of the two mechanisms is most pronounced in its own field and temperature ranges. The first mechanism is a negative MR effect with a sharp peak at zero fields: the resistance decreases as the magnetic field is increased. The negative MR effect resembles the typical giant MR (GMR) effect as it occurs in granular GMR or layered multilayer structures [72, 73, 74]. In this case, in the absence of an applied magnetic field, the magnetization in adjacent ferromagnetic grains/clusters or layers is antiparallel due to a weak anti-ferromagnetic coupling.

For the pristine phase, the negative MR was detectable only at low temperatures, up to approximately 100 K while the positive MR prevailed at room temperature. On the contrary, the functionalized phase showed a stronger negative MR also at room temperature. The negative MR as an indicator of an anti-parallel spin alignment together with the presence of non-zero remnant magnetization as will be described in Chapter 4 indicated that a mixed state that combines parallel and anti-parallel spin alignments might

be characteristic to the magnetic properties observed in the functionalized graphene sample at room temperature.

Figure 3-7 shows the MR in an out-of-plane direction for a set of temperature values from 2 to 300 K for the pristine and functionalized phases, respectively. As the applied field is increased, the magnetization in the adjacent regions aligns parallel. The resulting reduction of electron scattering is reflected in the observed decrease of the resistance. The above measurements indicate that for the "pristine" graphene sample the negative MR effect is best observed in a relatively low-field field range, from -1 to +1 kOe, and at the lowest temperature, 2K, and gradually disappears as the temperature is increased above approximately 100 K. The value of the negative MR is approximately 1 % at 2 K.

The second mechanism is a positive MR effect, i.e. the resistance increases as an external field is increased. It is displayed in the entire temperature range of interest and most distinguished at room temperature when the negative MR disappears. It could be observed that the effect reminds the magnetoresistance in a semiconductor with a single carrier type for which the resistance is proportional to $(1+(\mu H)^2)$ where μ is the carrier mobility [75]. The main difference between the pristine and functionalized phases is the fact that in the functionalized case the negative MR effect is pronounced in a greater field range and at higher temperature values. The noticeable field range of the negative MR effect for the functionalized phase extends substantially above 1 kOe while the characteristic temperature at which the MR changes from negative to positive is above room temperature, compared to less than 80 K for the pristine phase.

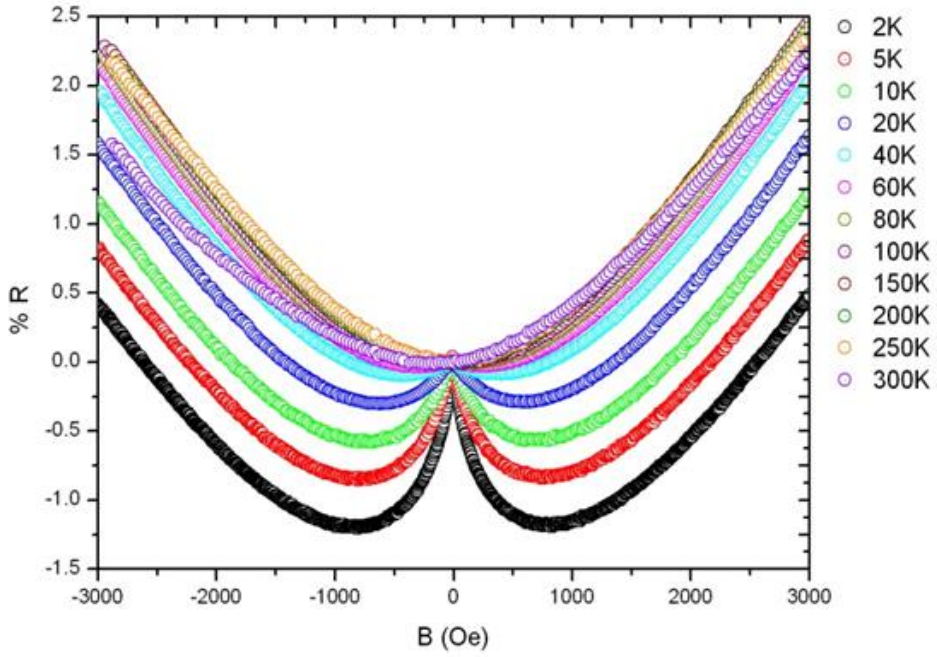

(a)

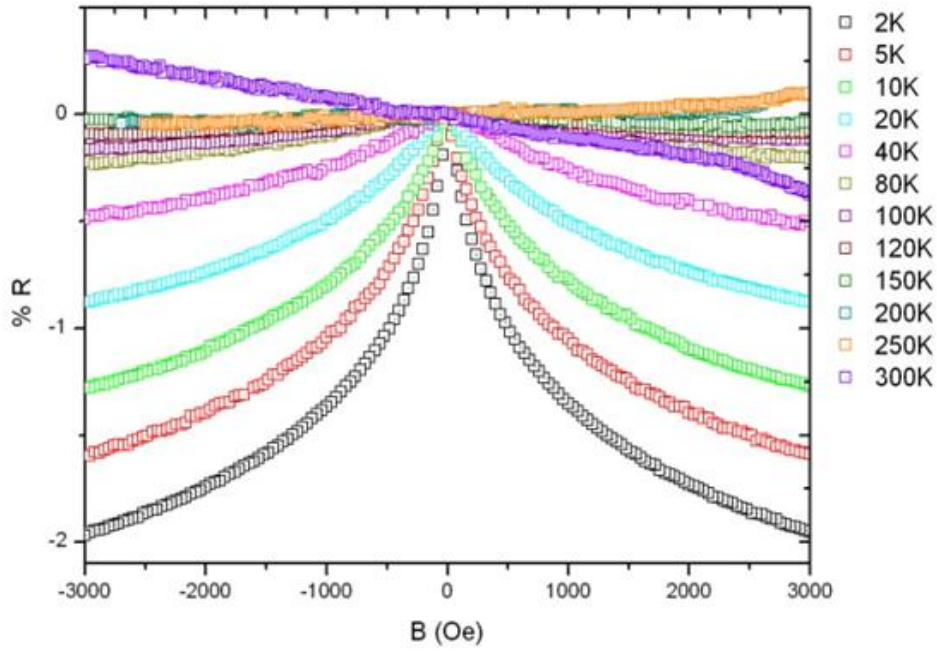

(b)

Figure 3-7 Out-of-plane magnetoresistance for a set of temperature values from 2 to 300 K for (a) the pristine and (b) functionalized phases.

The MR curves at room temperature for a set of 11 values of the tilt angle, from 0 to 90^0 with a step of 10^0, respectively, which is defined as the angle between the magnetic field and the normal to the graphene sheet, are shown for the pristine and functionalized phases in Figure 3-8 (a) & (b), respectively. These measurements indicate significant anisotropy of the MR signal, with barely any dependence at a 90-degree angle equivalent to the field in the plane of the graphene sheet.

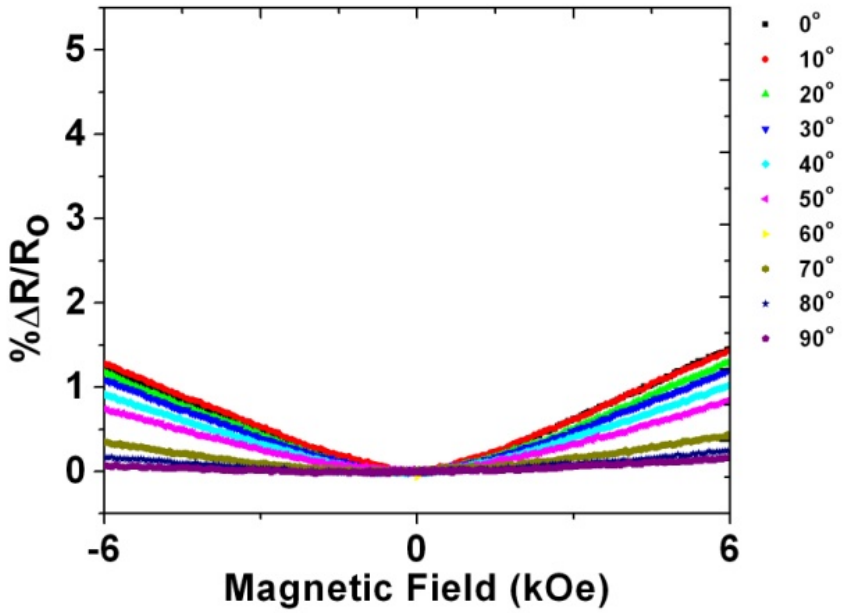

(a)

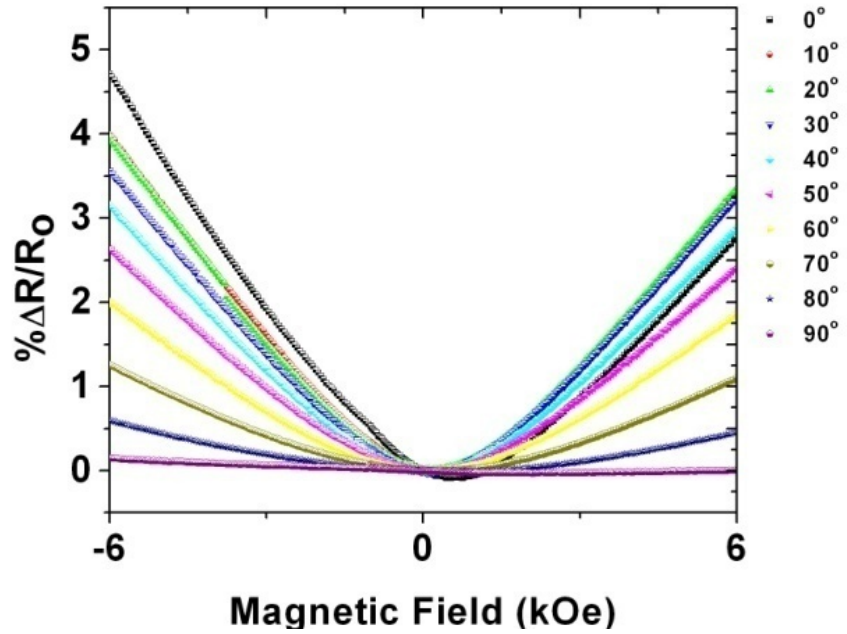

(b)

Figure 3-8 Anisotropy of in-plane (a) and out-of-plane (b) spin alignment

To better understand the anisotropy effects in graphene samples, the magnetoresistance was measured also in an in-plane direction. The out-of-plane and in-plane MR measurements for a set of temperature values from 2 to 300 K for the pristine phase are shown in Figure 3-9 (a) and (b), respectively.

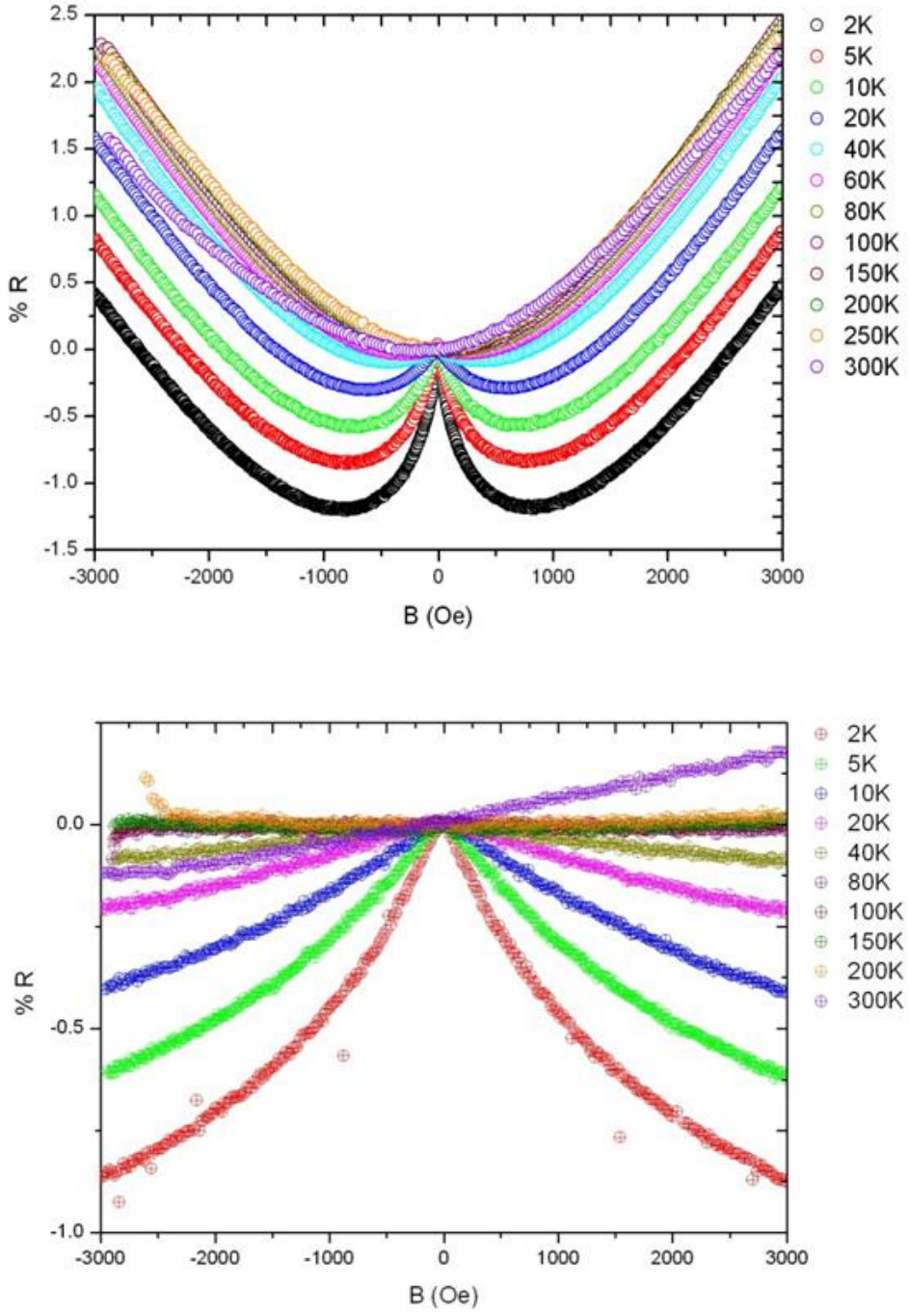

Figure 3-9 (a) Out-of-plane and (b) in-plane magnetoresistance for a set of temperature values from 2 to 300 K for the pristine phase.

The key observation is the fact that in the in-plane direction only the negative MR effect is observed. Assuming the origin of the negative MR is similar to that of GMR observed in granular and layered magnetic structures, the characteristic field at which the MR disappears might be attributed to the field necessary to switch coupling between adjacent magnetic sites from anti-parallel to parallel alignment. Putting this together with the earlier discussed results from M-H measurements, we can conclude that the magnetic properties of the sample at room temperature are defined by a mixed state that combines regions with anti-parallel and parallel spin alignments.

Finally, it was observed that in the in-plane orientation, the negative MR makes a dominant contribution to the net MR while in the out-of-plane orientation both negative and positive MR effects make essential contributions. The anisotropy observed in both MR and M-H measurements was associated with the 2D nature of the graphene structure.

3.4 **Scanning Tunneling Microscopy (STM)**

Understanding the role of defects such as functionality and other mechanical defects in the transport properties of graphene is important to realizing carbon-based future electronics. Using scanning tunneling spectroscopy, researches [76] have observed quasiparticle interference patterns in epitaxial graphene grown on silicon carbide. The study of scanning tunneling microscopy of graphene is extremely important not only for

figuring out the relationship between the origin of magnetism and the functionality, but electronic properties of graphene with functionalization in general. STM under ambient condition was performed by STM module from Veeco Instruments [77]. To image single layer graphene and amorphous carbon films on conductive substrates under ambient condition Pt-Ir tips were employed.

From the theory, Scanning Tunneling Microscopy relies on tunneling current between the probe and the sample to sense the topography of the sample. A sharp metal tip such as Pt-Ir and Tungsten, in this project, Pt-Ir is used for the STM probe. Then it is positioned a few atomic diameters above a conducting sample which is electrically biased with respect to the tip. At a distance under 1 nanometer, a tunneling current will flow from the sample surface to the tip. When it is in operation, the bias voltages typically range from 10 to 1000mV while the tunneling currents vary from 0.2 to 10 nA.

The tunneling current changes exponentially with the tip-sample separation, and typically it is decreasing by a factor of 2 as the separation is increased by 0.2 nm. The tunneling current, *I* has a very important characteristic: it exhibits an exponentially decay with an increase of the gap, *d* like $I= KUe^{-(kd)}$ where capital and lower case letters, *K* and *k* are constant values and U is the tunneling bias. The exponential relationship between the tip separation and the tunneling current makes the tunneling current an excellent parameter for sensing the tip-to-sample separation as shown in Figure 3-10. In essence, a reproduction of the sample surface is produced by scanning the tip over the sample surface and sensing the tunneling current.

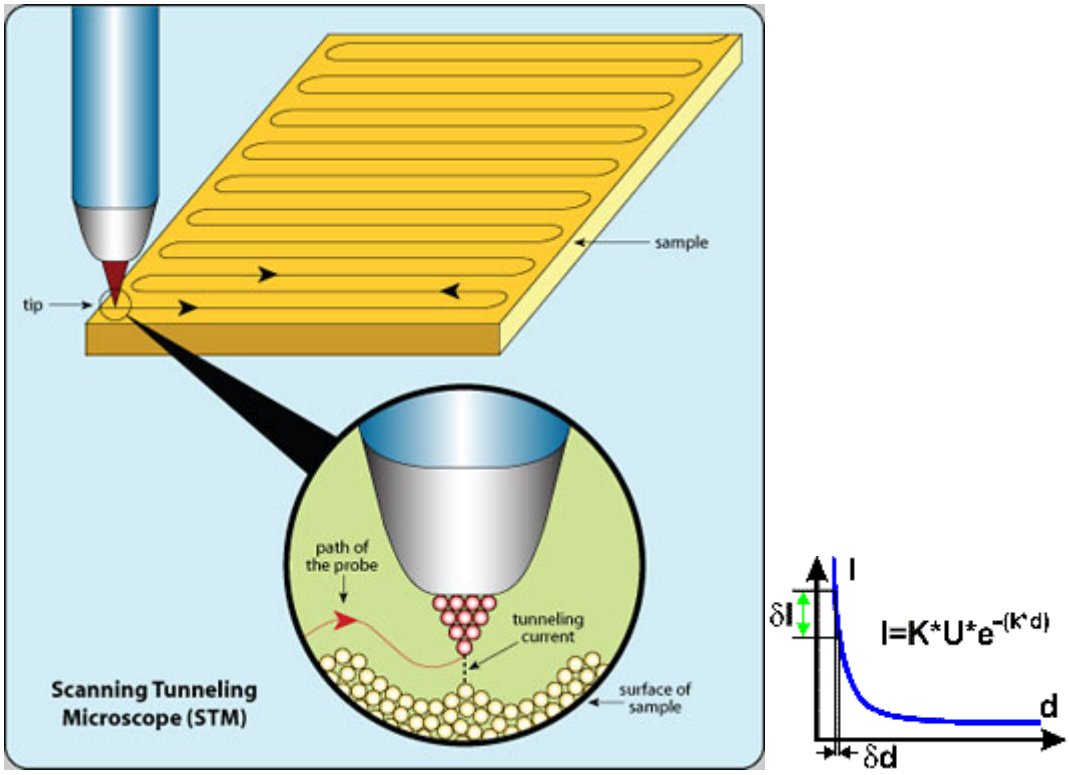

Figure 3-10 Brief principle of scanning tunneling microscopy system; this could be represented by the equation: $I \sim KUe^{-kd}$ (where I = Tunneling current, U = Bias voltage between tip and sample, k = constant, and d = tip-sample separation distance).

The sample is positively or negatively biased so that the tunneling current flows when the tip is in contact to the sample. With the help of the tunneling current, the distance between tip and sample is constant. If the tunneling current exceeds its pre-set

value, the distance between tip and sample is decreased. Meanwhile, if it falls below this value, the feedback increases the distance.

The tip is scanned line by line above the sample surface following the topography of the sample. The reason for the extreme magnification capabilities of the STM down to the atomic scale can be found in the physical behavior of the tunneling current. The tunneling current flows across the small gap that separates the tip from the sample, a case that is forbidden in classical physics but that can be explained by the better approach of quantum mechanics: the electrons are “tunneling” across the gap.

Therefore, very small changes in the tip-sample separation induce large changes in the tunneling current. This has the consequences that the tip-sample separation can be controlled precisely and the tunneling current is only carried by the outermost atom of the tip. The atoms that are second nearest carry only a negligible amount of the current. So, the sample surface is scanned with a single atom theoretically.

As shown in Figure 3-11 [78], STM consists of scanner and controller electronics. From the fundamentals of STM as discussed, it basically allows the investigation of electrically conducting surfaces down to the atomic scale. The sample under the STM is scanned by a very fine metallic tip which is mechanically connected to the scanner, positioning device followed by Cartesian coordinates realized by means of piezoelectric materials.

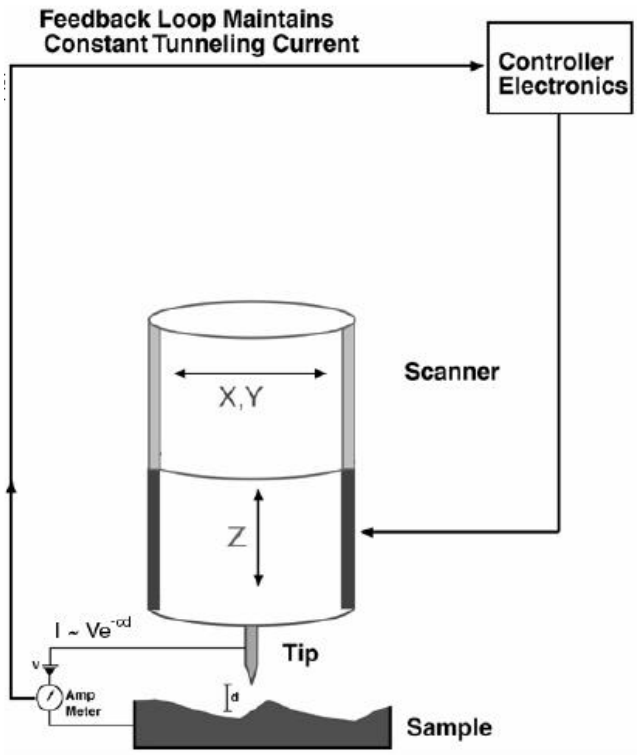

Figure 3-11 Apparatus of scanning tunneling microscopy system from Veeco [78]

The NanoScope STM is a digitally-controlled instrument capable of producing high resolution, three-dimensional images. The sample is held in position while a piezoelectric crystal in the form of a cylindrical tube scans the sharp metallic probe over the surface in a raster pattern. The digital signal processor (DSP) calculates the desired separation of the tip from the sample by sensing the tunneling current flowing between the sample and the tip. The bias voltage applied to the sample encourages the tunneling current to flow. The DSP completes the digital feedback loop by outputting the desired voltage to the piezoelectric tube.

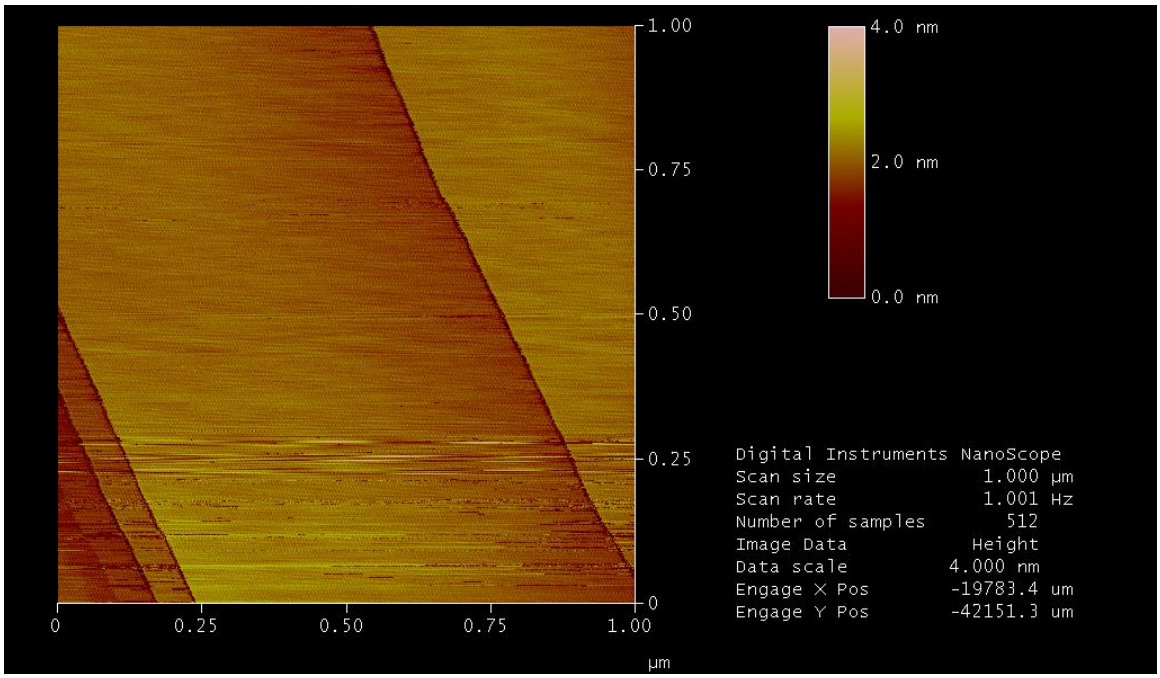

Figure 3-12 Scanning Tunneling Microscopy of graphitic films surface

The topography of graphitic films was shown in Figure 3-12. In the smaller region of the surface, the layered graphitic films were clearly observed with the much higher resolution. Only topography is shown in this dissertation since the research is still under confidential issue with spectroscopy studies such as local density of state and local I-V characteristics of functionalized graphene. After it is cleared, it will be reported in future communications with the current findings.

4. Magnetism of Graphene

4.1 Introduction

Conventional wisdom believes “magnetic materials have to contain some metallic atoms with partially filled d- or f- orbitals.” However, the discovery of a type of pure carbon that is magnetic at room temperature in 2002 [79] is bound to invite controversy. Then, so far theoretical researches predict a whole spectrum of magnetic phenomena in graphene including several mechanisms for intrinsic ferromagnetism and spin-ordering effects that arise due to the nature of its dimensionality. However, none of these effects has so far been explored experimentally. However, recent studies show that ferromagnetism of graphene itself and the chemically modified graphene by covalent attachment of aryl groups to the basal plane of carbon atoms was found. Epitaxial graphene with functionalization form may make a role of magnetic semiconductor.

The existence of spin ordering in graphene will have important implications not only for understanding this remarkable material with chemical functionalization form, but for its various applications: magnetic semiconductors and the field of spintronic devices such as new information processing and data storage devices. With these unconventional materials such as fullerenes, bulk graphite, and graphene, ferromagnetism has been detected in spite of the absence of atoms that have non-zero total spin, but the findings remain highly controversial and there are many uncertainties related to the experimental system with and/or without any crystal defects and impurities. Therefore, it should allow clear answers to questions related to magnetism in other graphitic materials, in which the

inevitable presence of impurities and imperfections can obscure vital evidence or lead to artifacts.

Here, the VSM measurements made it completely to pull out magnetic properties of pristine and functionalized graphene samples. The characteristic shape of the M-H hysteresis loops indicated contributions from both ferromagnetic and antiferromagnetic regions, with the preferred easy axis normal to the plane of the graphene sheet. In order to support the bulk measurements, low density functionalized samples with atomic force microscopy (AFM) and magnetic force microscopy (MFM) measurements were examined by as-developed high sensitive probe and found that it could be directly correlated with the chemically functionalized regions to the high-density magnetic regions of the graphene layer. Optimal micro-optical Kerr effects microscopy (MOKE) system (MOKE) to study the local spin polarization will be discussed about the chemical functionalization of this carbon material.

4.2 **Bohr Magneton of Carbon Atoms**

In quantum mechanics, the Bohr Magneton is used for a physical constant of magnetic moment of electrons per single atom. The Bohr Magneton which is expressed as "μ_B" is natural unit for expressing an electron magnetic dipole moment. An electron has intrinsic magnetic dipole moment of approximately one Bohr Magneton [80]. The study of Bohr Magneton of single carbon atom is critical because it will verify how many Bohr Magneton single carbon atom contains.

Bohr Magneton Calculation of graphene structure is started from the unit area of the carbon atoms as shown in Figure 4-1.

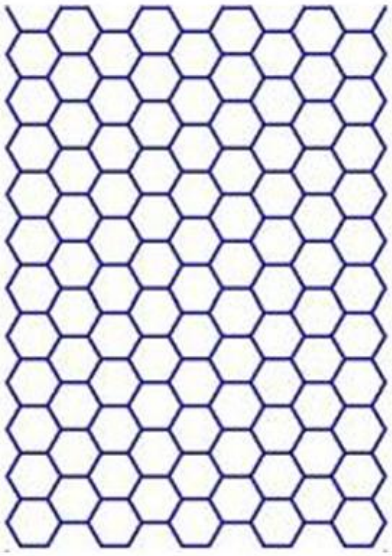

The standard length of C-C bond |a| = |b| = 1.421 Å

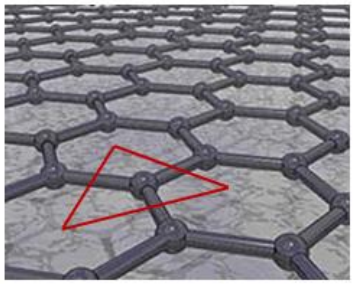

$$C_C = \frac{4}{\sqrt[3]{3^2}} a^{-2} = 3.81 \times 10^{15} \, atoms / cm^2$$

where a is the carbon-carbon bond length in graphene (a = 0.1421nm).

The effective magnetic moment per carbon:

$$\mu_{eff} = M_{sat} \times V/N_C = 9.2 \times 10^{-22} \text{ emu} = 0.1 \, \mu_B$$

Figure 4-1 Chicken wire shape made of carbon atoms and C-C bond of graphene; the concentration of carbon atoms in unit area are is 3.81 × 10^{15} atoms/cm^2.

From the magnetization value, the sample area, volume and the number of carbon atoms in the functionalized monolayer should be calculated in advance. The concentration of carbon atoms per unit area is given by $C_C = (4/3^{3/2}) a^{-2} = 3.81 \times 10^{15}$ atoms/cm^2, where *a* is the carbon-carbon bond length in graphene (*a* = 0.1421nm) [81]. The area of the

sample is given by $A = 0.371$ cm^2, where the functionalized monolayer covers all surfaces of the $0.45 \times 0.35 \times 0.035$ cm^3 of Silicon Carbide substrate. Thus, the volume of the functionalized EG sample is $V = 1.3 \times 10^{-8}$ cm^3, where the thickness of the layer of functionalized carbon is taken to be 0.35 nm; the number of carbon atoms in the active layer is $N_C = C_C \times A = 1.41 \times 10^{15}$. A representative value of the saturation magnetization of functionalized graphene at room temperature is $M_{sat} = 1.3 \times 10^{-6}$ emu and thus, the effective magnetic moment per carbon is given by $\mu_{eff} = M_{sat}/N_C = 9.2 \times 10^{-22}$ emu = 0.1 μ_B.

Considering that there are approximately five carbon atoms per nitrophenyl group in functionalized graphene [48, 49], each functionalized site contributes approximately 0.5 μ_B to the sample magnetization. It is important to note that based on an estimate of 5 total layers of graphene in the pristine EG sample and a representative value of the saturation magnetization for EG of $M_{sat} = 0.3 \times 10^{-6}$ emu, the effective magnetic moment per carbon atom in EG is $\mu_{eff} \approx 0.005$ μB; thus functionalization increases the magnetism of the graphene carbon atoms by a factor of 20 although impurities could not be excluded as the origin of the very small signal in pristine EG.

4.3 **Vibrating Sample Magnetometer**

Vibrating Sample Magnetometry (VSM) experiments of graphene and the interactions between single layer of graphene and ferromagnetic materials such as Cobalt are done by the Quantum Design VSM option for the Physical Property Measurement

System (PPMS) [82]. VSM option is a fast and sensitive DC magnetometer. The basic measurement is accomplished by oscillating the sample near a detection coil, which is called as pick-up coil, and synchronously detecting the voltage induced. By using compact gradiometer pickup coil configuration, relatively large oscillation amplitude (1-3 mm peak) and a frequency of 40 Hz, VSM is able to resolve magnetization changes of less than 10^{-6} emu at a data rate of 1 Hz.

As shown in Figure 4-2, PPMS consists of Probe and dewar jackets for liquid Nitrogen and liquid Helium outside of the probe. PPMS Probe consists of superconducting solenoid Magnet which could be reached up to 14 T, thermometer, and others as indicated below. VSM consists primarily of a VSM linear motor transport for vibrating samples, a coil set puck for detection, electronics for driving the linear motor transport and detecting the response from the pickup coils. MultiVu software applies for automation and control.

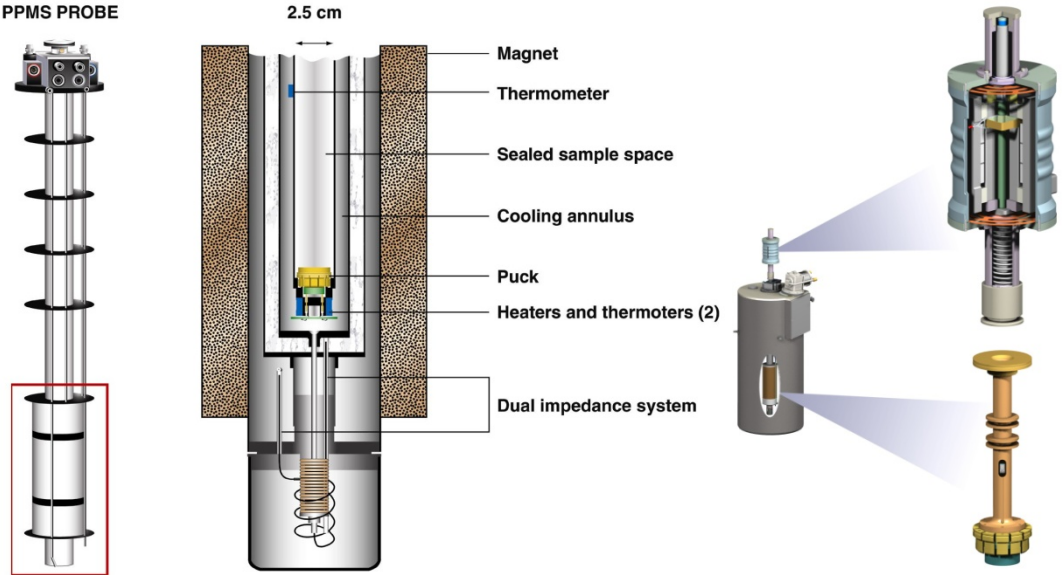

Figure 4-2 VSM system for the PPMS: PPMS probe (L) image and detailed cross sectional view of the probe. PPMS probe consists of superconducting solenoid magnet up to 14 T. VSM linear motor module (R) and pick up coilset on the bottom [83].

Although VSM is commercially available system, the obstacles are how to operate it with highest sensitivity to pull out magnetic signal of the samples precisely so that the physical phenomena of graphene with VSM could be clearly obtained. The block diagram of VSM is shown in Figure 4-3. A dipole moment will be induced if a sample of any material is placed in a uniform magnetic field, created between the poles of an electromagnet. The sample will start to vibrate with sinusoidal motion and a sinusoidal electrical signal can be induced in suitable placed pick-up coils. The signal has the same

frequency of vibration and its amplitude will be proportional to the magnetic moment, amplitude, and relative position with respect to the pick-up coils. The Model 6000 controller manage sample space, annulus vacuum, dewar gas, vacuum pump, and magnet power supply.

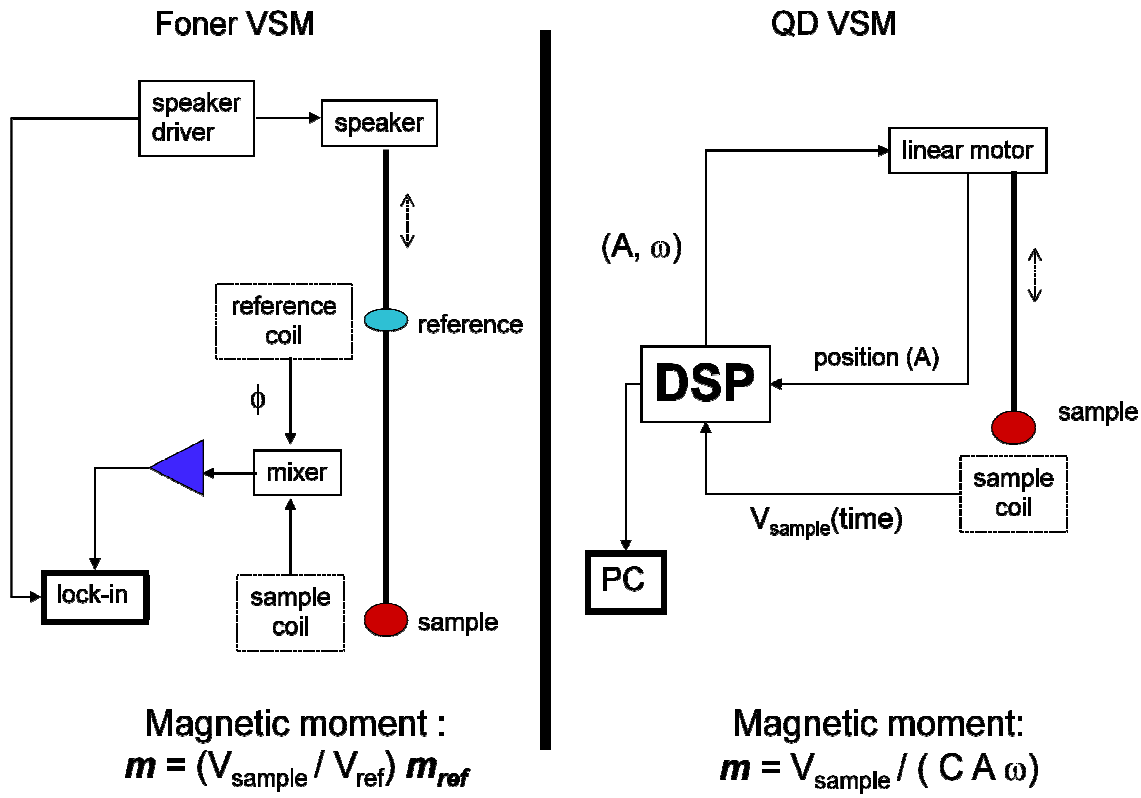

Figure 4-3 VSM block diagram; the comparison between Foner VSM which is traditional VSM (L) and VSM from QD for this project (R) is shown.

The sample is fixed to a small sample holder located at the end of a sample rod mounted in an electromechanical transducer. The transducer is driven by a power

amplifier which itself is driven by an oscillator at a frequency of 40 Hz. Then, the sample vibrates along the Z-axis perpendicular to the magnetizing field. The latter induced a signal in the pick-up coil system that is fed to a differential amplifier. The output of the differential amplifier is subsequently fed into a tuned amplifier and an internal lock-in amplifier that receives a reference signal supplied by the oscillator. The output of this lock-in amplifier, or the output of the magnetometer itself, is a DC signal proportional to the magnetic moment of the sample being studied.

The samples were mounted on the quartz paddle holder for In-Plane measurements with GE-7031 varnish to withstand thermal cycles from the measurements. To optimize the touchdown process, the samples were mounted with the offset of 35 mm from the bottom. For Out-of-Plane measurements, quartz holder with GE-7031 varnish was used. Background magnetic measurements were checked for empty holders and Silicon Carbide. 3 kOe and 6 kOe of field with 10.13823 Oe/sec of sweep rate were applied for In-Plane and Out-of-Plane measurements, respectively. From 2 to 300 K, the sample was installed in the PPMS chamber and the field dependence of magnetization was measured.

With the goal to eliminate the contribution into the vibrating sample magnetometry (VSM) signal of the effects due to substrates and sample holders, the following measurement sequence was applied. First, after SiC background measurement, SiC substrates (on which graphene layers were epitaxially grown) generated negligible magnetic signal. Then, M-H loops for the graphene in the pristine stage were performed. To find the magnetization, total volume of the sample was calculated with the number of carbon layers (5 to 10 depending on a sample). Finally, MH-loops for the same graphene

sample after the chemical functionalization were measured. Because the functionalization affects the top surface only, the change in the magnetic signal occurred only due to the top graphene layer. To find the signal due to the functionalized region, it was subtracted from the net measured signal due to the pristine stage, as found in the previous step. Finally, to eliminate the possibility of iron based impurities, we conducted an EPR study which confirmed the absence of iron compounds.

The derived from M-H loops temperature dependence of the saturation magnetization for the functionalized sample is shown in Figure 4-4. The irregular temperature dependence also indicates the presence of antiferromagnetically coupled regions for the two NP-EG functionalized samples; apparently the Curie temperature of NP-EG is above room temperature.

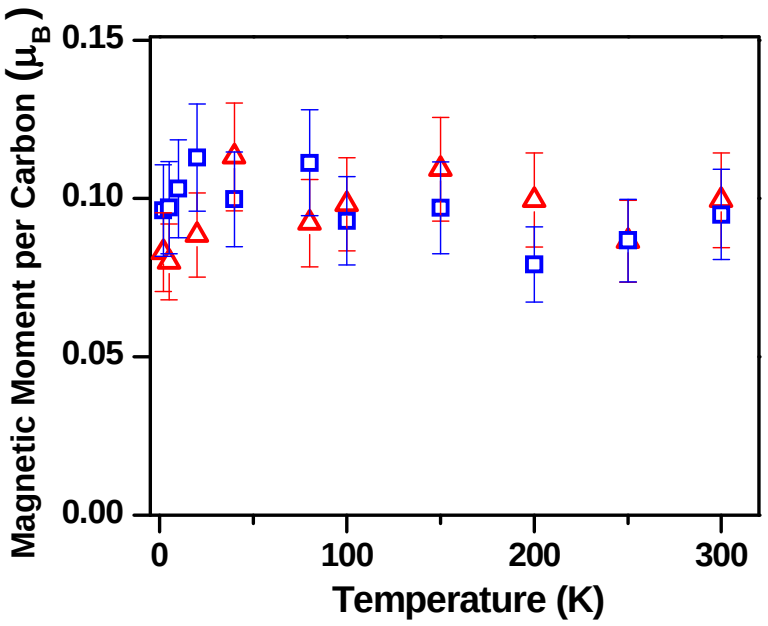

Figure 4-4 Temperature dependence of the saturation magnetization per carbon atom expressed in Bohr magneton for two different functionalized graphene.

The measured magnetization-versus-field (M-H) hysteresis loops in a temperature range from 2 to 300 K for the two key orientations of the magnetic field, in-plane and out-of-plane, respectively. Both in-plane and out-plane measurements showed a relatively small value for the saturation magnetization for the pristine stage. In the entire temperature range under study, the saturation magnetization was below 1 emu/cc. The functionalization boosted the value above 100 emu/cc at room temperature. As a result, the signal in the pristine stage appeared negligibly small on the scale suitable for the

functionalized stage. Therefore, in Figure 4-5 (a), the inserts show a magnified view of the respective M-H loops in the pristine stage. The summarizing M-H loops at a set of five different temperature values, 2, 10, 40, 250, and 300 K, respectively, for the in-plane measurements at the pristine (a) and functionalized stages (b) and the out-of-plane (c) measurements at the functionalized stage are shown in Figure 4-5, respectively.

The room-temperature value of approximately 100 emu/cc for the saturation magnetization corresponds to approximately 0.1 μ_B (Bohr magnetons) per carbon atom as described in Section 4.2. Considering that there were approximately five carbon atoms per one functionalized entity, each functionalized site contributed with approximately 0.5 μ_B. For comparison, for the ferromagnetic iron, the saturation magnetization is approximately 2.2 μ_B per atom.

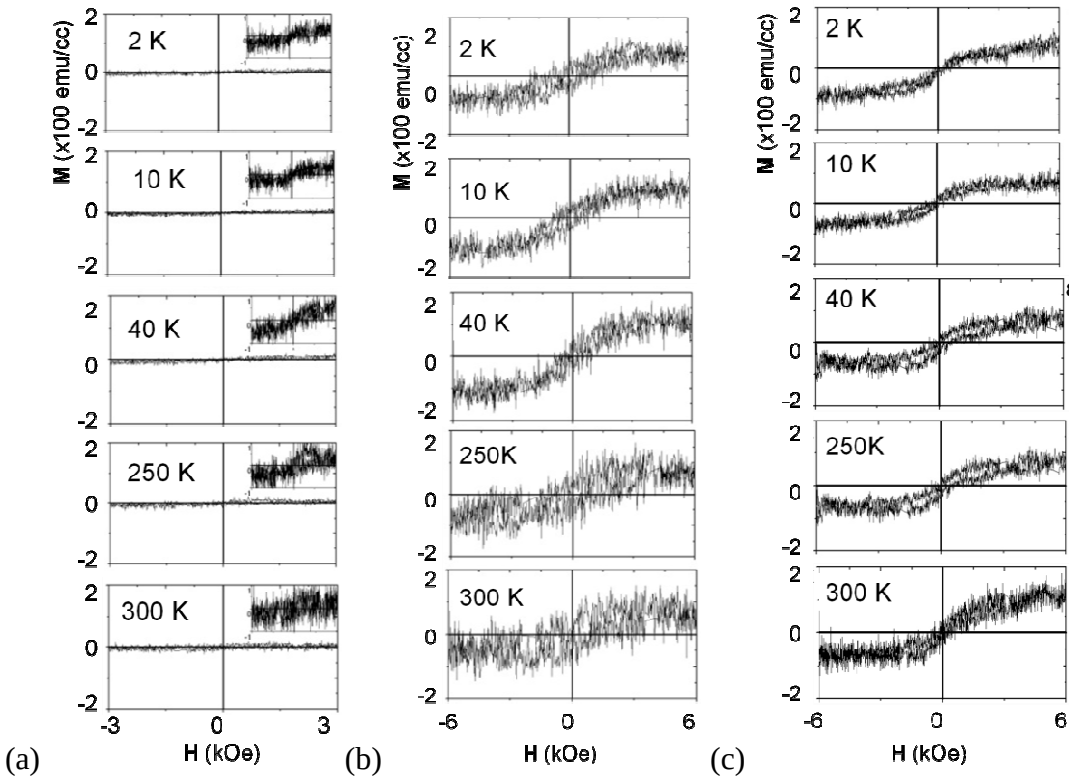

Figure 4-5 Overall M-H hysteresis loops at a set of five temperature values, 2, 10, 40, 250, and 300 K, respectively, for (a) the in-plane measurements at the pristine stage (with inserts' scale magnified 50 times) and (b) the functionalized stage and (c) the out-of-plane measurements at the functionalized stage.

Another observation relates to the type of the long-range magnetism in the sample under study. As indicated in Figure 4-5 (b) and (c), the presence of antiferromagnetic regions may be significant. The in-plane measurements show hysteresis loops similar to typical loops for normal either ferromagnetic or antiferromagnetic material, with some remnant magnetization and an "easy" axis normal to the plane. However, the out-of-plane

measurements display no significant remnance and show double loops typical to antiferromagnetically coupled materials with the “easy” axis normal to the plane. These will illustrate the sequences of the spin switching (in the antiferromagnetic region) in later chapter, as the field is applied in in-plane and out-of-plane directions, respectively.

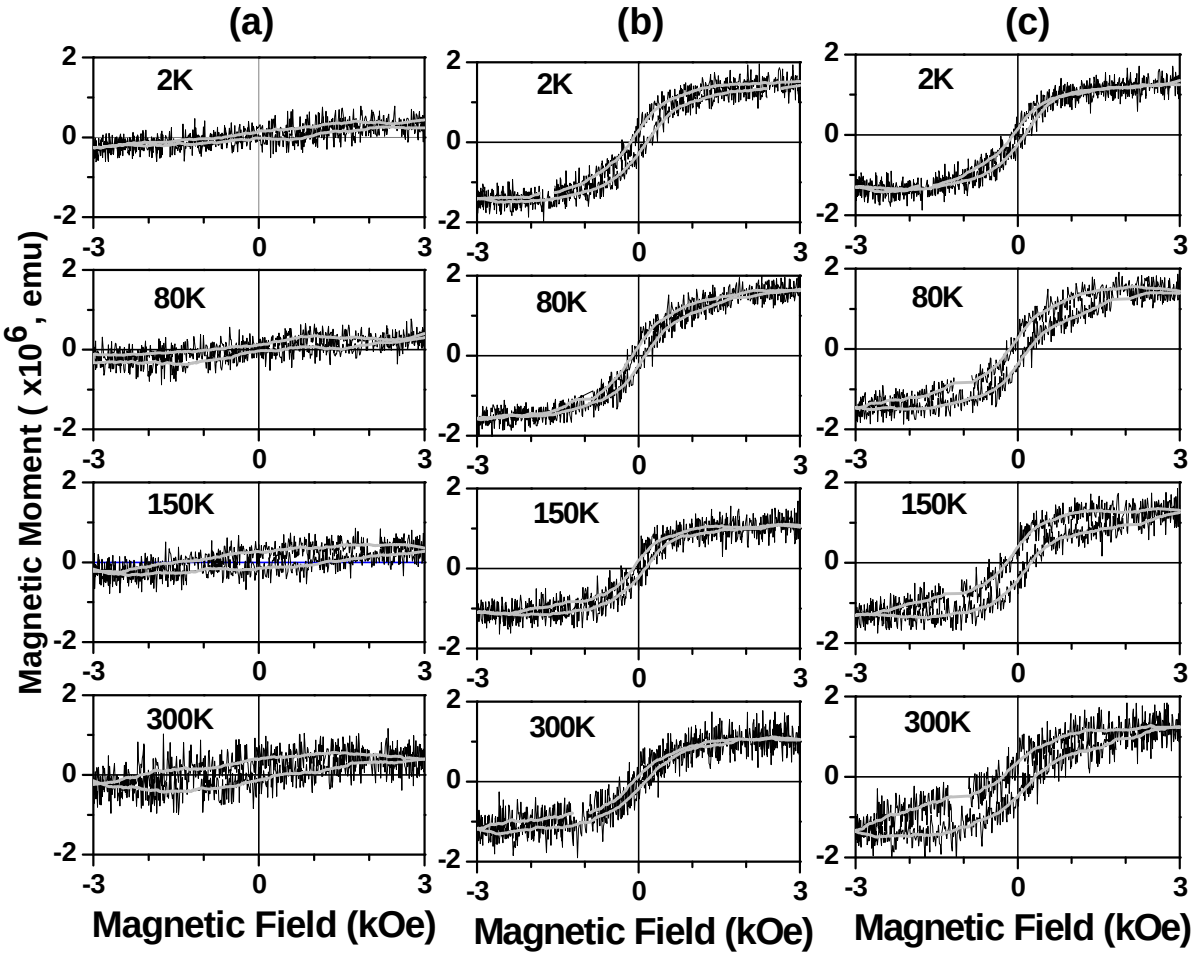

Figure 4-6 M-H hysteresis loops of In-Plane measurement at a set of four temperatures, for (a) pristine EG, (b) functionalized EG, and (c) functionalized EG after subtraction of the magnetic moment of pristine EG. Gray lines show M-H loops after smoothing.

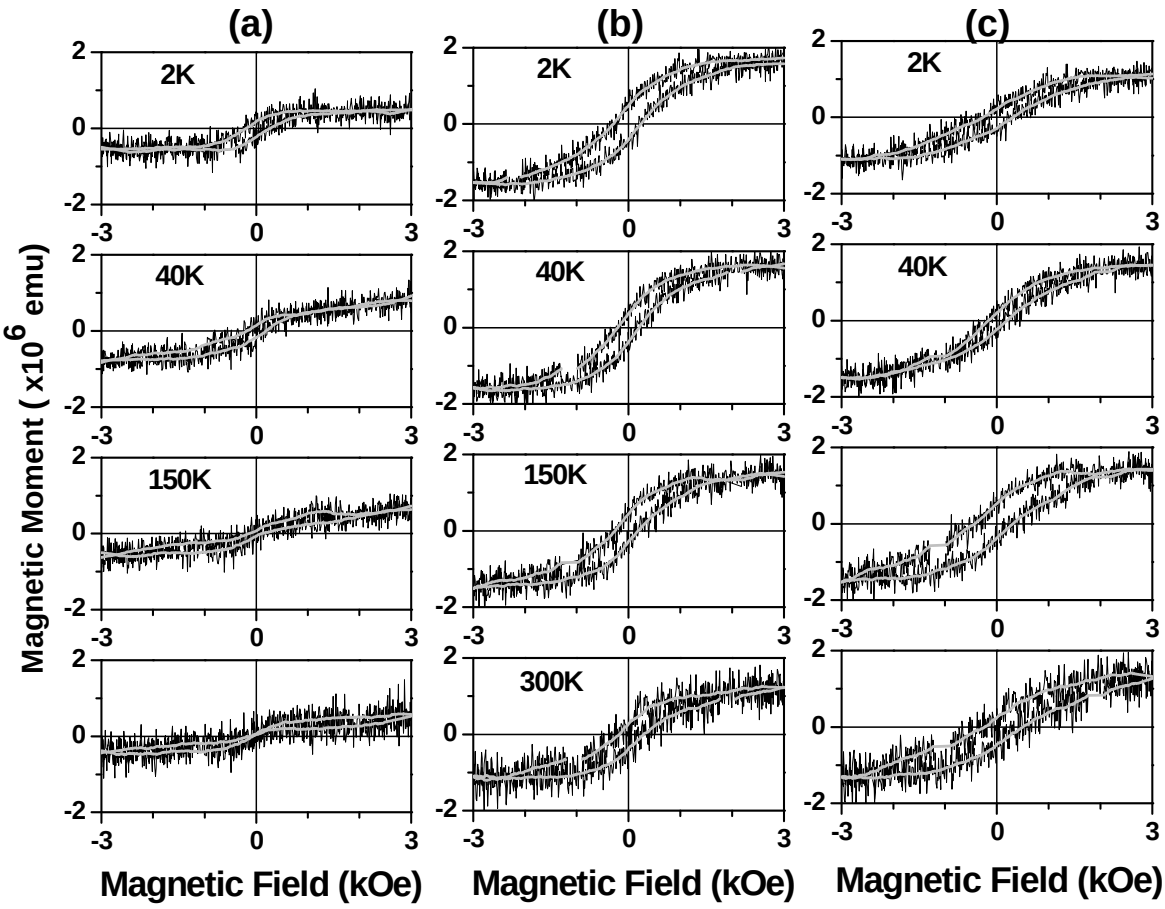

Figure 4-7 M-H hysteresis loops of In-Plane component at four temperature ranges for a different sample. (a) pristine EG, (b) functionalized EG, and (c) functionalized EG after subtracting the magnetic moment of pristine EG. Gray lines show M-H loops after smoothing the noise.

The detailed M-H loops for the in-plane measurements of the pristine (EG) and functionalized (NP-EG) samples are shown in Figures 4-6 and 4-7; the M-H loops were obtained after linear subtraction of the diamagnetic background signal. The in-plane

measurements show hysteresis loops with some remnant magnetization which are characteristic of a mixed state of ferromagnetic and antiferromagnetic coupling. The in-plane measurements showed a relatively small value for the saturation magnetization of the entire pristine (EG) sample over the full temperature range ($M_S < 0.5 \times 10^{-6}$ emu), whereas functionalization of the topmost monolayer increased the observed signal to $M_S > 1 \times 10^{-6}$ emu over the entire temperature range.

In summary, the most important observation from the described measurements is the strong effect of functionalization on the magnetic properties of epitaxially grown graphene. After the ultra-high-density chemical functionalization, graphene samples not only became semiconducting at room temperature but also displayed high-density room-temperature magnetism, with the saturation magnetization of 0.1 Bohr magnetons per carbon atom. The anisotropic magnetic properties (with the antiferromagnetic "easy" axis normal to the plane) may be associated with the 2D nature of graphene samples.

4.4 **Magneto-Optical Kerr Effects**

The idea of Magneto-optic Kerr effect (MOKE) microscopy is to detect the changes of laser which is reflected from magnetized media. Both polarization and reflectivity could be changed from the reflected laser beam from a magnetized surface. Kerr effect is identical to the Faraday effects which are a measurement of the transmitted light. Meanwhile, the magneto-optical Kerr effect is a measurement of the reflected beam. Both effects result from the off-diagonal components of the dielectric tensor, ε.

MOKE can be categorized by the direction of the magnetization vector with respect to the reflecting surface and the plane of incidence such as polar, longitudinal, transversal, and focus MOKE. MOKE is the key operation principle of magneto-optical drives and is called as Kerr microscopy to visualize the magnetic domain structure of a sample. Kerr microscopy is an optical light microscope with an additional polarizer and an analyzer to obtain a different contrast from different magnetic orientation.

When the magnetization vector is perpendicular to the reflection surface and parallel to the plane of incidence, the effect is called the polar Kerr effect. To simplify the analysis, near normal incidence is usually employed when doing experiments in the polar geometry. P-MOKE stands for perpendicular or polar (out-of-plane) as opposed to longitudinal (in-plane) L-MOKE. The schematics of P- and L-MOKE are shown in Figures 4-8 and 4-9, respectively.

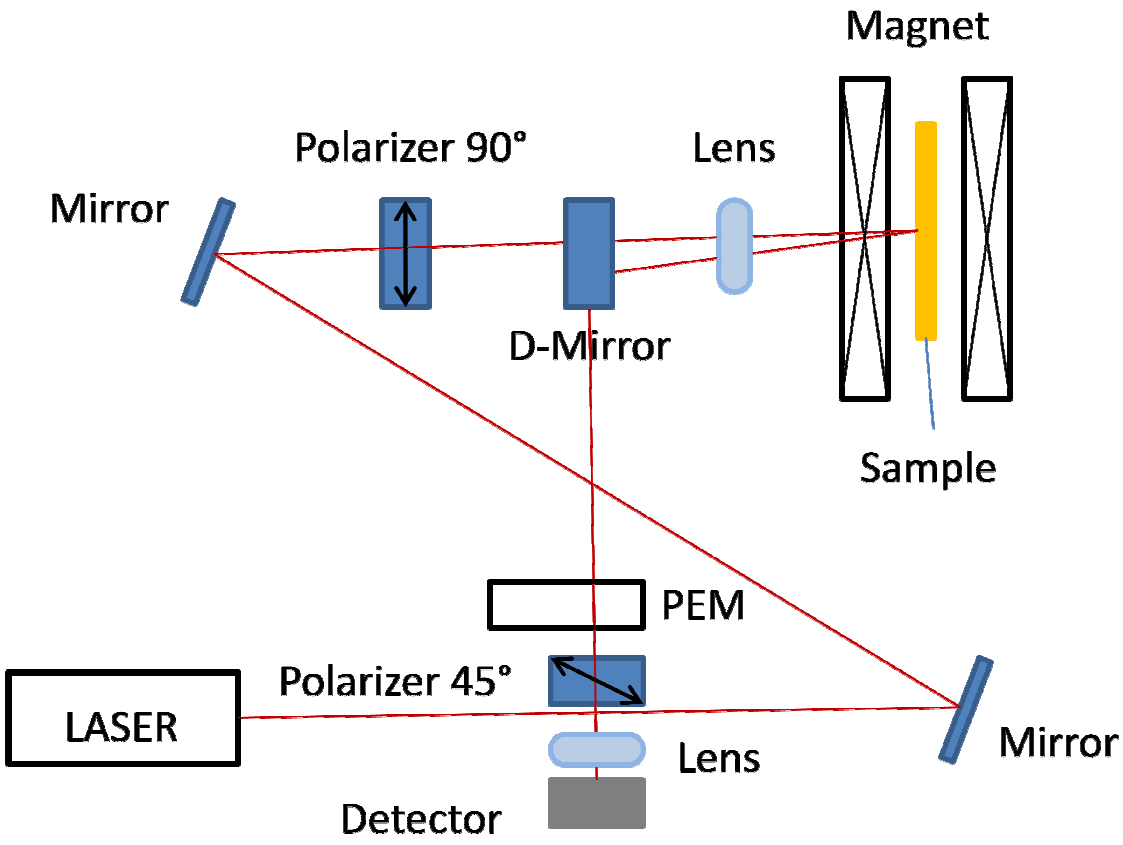

Figure 4-8 Schematics of Polar MOKE; the sample is located inside of electromagnet (yellow color).

The laser is directed to the sample located between the poles of an electromagnet which could reach up to 3T. Standard two-mirror setup as shown in Figure 4-8, allows to adjust both laser position and angle of incidence (in both vertical and horizontal directions) to ensure the laser focused by the lens and passing through a small hole into the electromagnet before laser touch the sample. The laser is polarized either vertically or horizontally by an adjustable 90° polarizer. The reflected laser passes through the lens

again, and then it is being deflected towards the photo-elastic modulator (PEM), the 45° polarizer, and the detector**.**

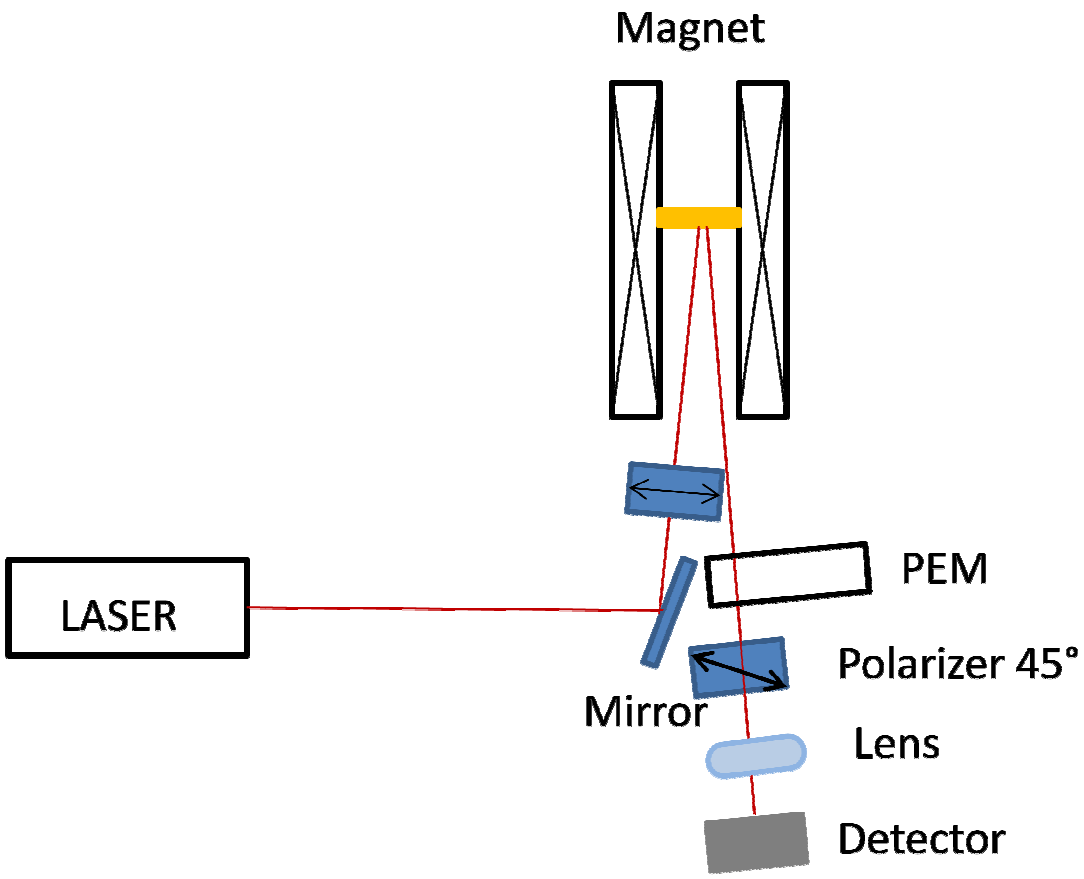

Figure 4-9 Schematics of Lateral MOKE; Polarizer 90° is located between mirror and sample (Blue box).

For L-MOKE set-up, the magnetization vector is parallel to both the reflection surface and the plane of incidence. The longitudinal setup involves laser reflected at an

angle from the reflection surface. Linearly polarized laser, incident on the surface, becomes elliptically polarized with the change in polarization directly proportional to the component of magnetization - that is parallel to the reflection surface and to the plane of incidence. This elliptically polarized laser has two perpendicular *E* vectors, called as the standard Fresnel amplitude coefficient of reflection, *r* and the Kerr coefficient, *k*. The Kerr coefficient is typically much smaller than the coefficient of reflection.

MOKE of graphene is important study because it could be possible to open the ways to observes optical effect and magnetic effect simultaneously. Laser detects the spots with different coverage of functionality. Because of the transparency of graphene, transmitted P-MOKE set-up needs to be applied as shown in Figure 4-10. The laser passes all layers just once so that the resulting signal is proportional to the total magnetic moment from all the layers. The focused laser converges near the focusing point of the objects (a con-focal configuration) in order for the laser to exit on the opposite side of the magnet without disturbance of laser from the walls of the magnet. Linear Faraday background signal created by the substrate is always present to be subtracted afterwards.

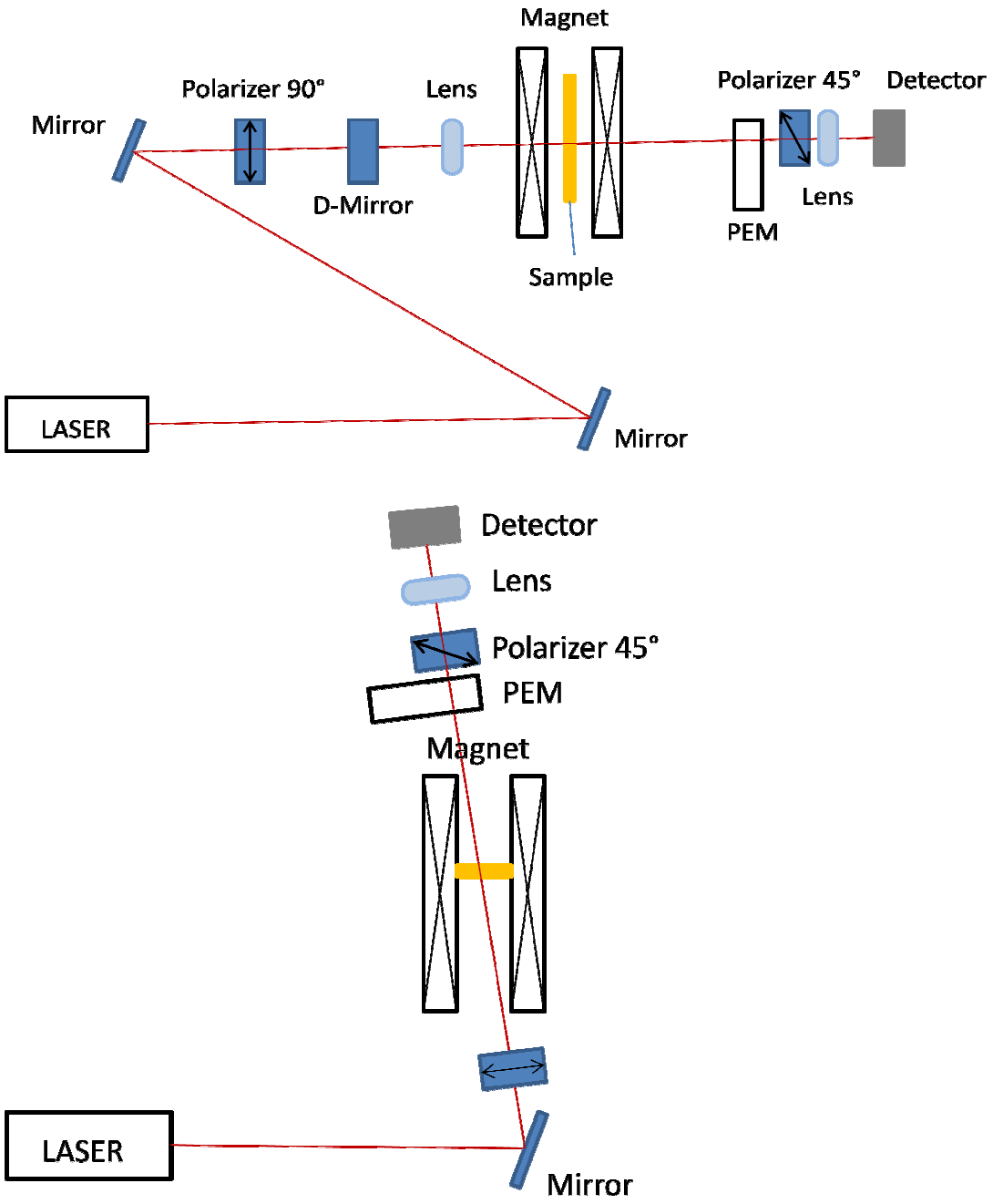

Figure 4-10 The Schematics of polar and lateral MOKE in transmission; the laser will be transmitted through the sample and so the detector is located behind the sample.

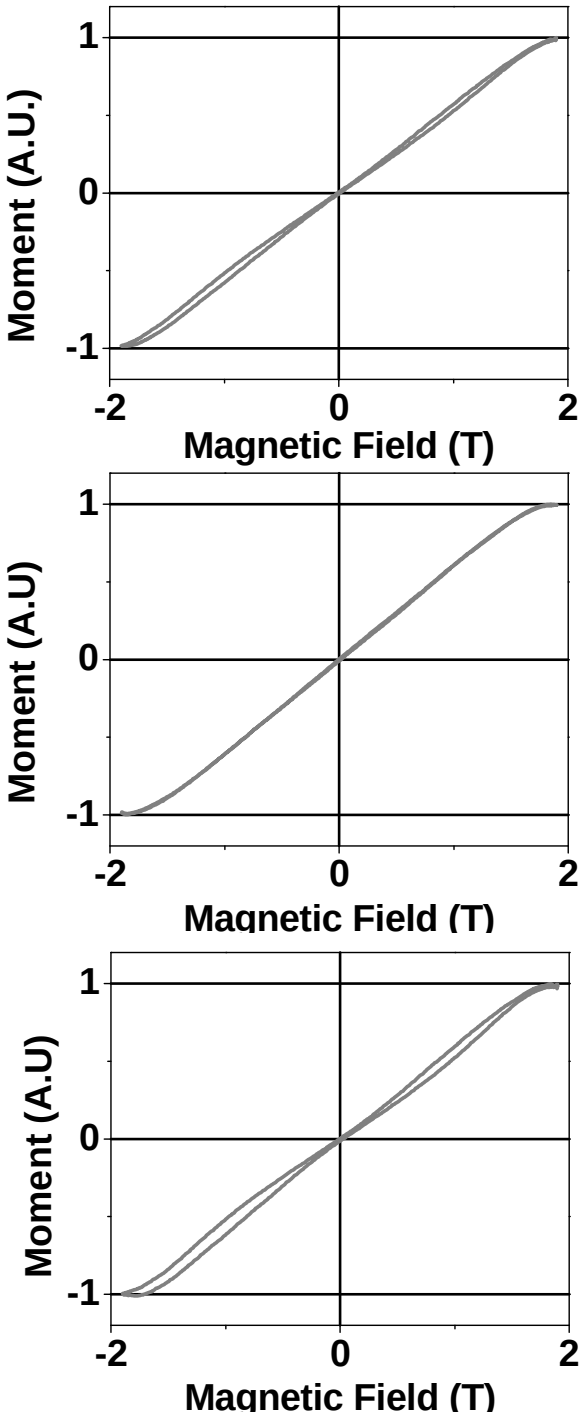

Figure 4-11 Kerr Signal from P-MOKE of functionalized EG with different spots: 1, 2, and 3, respectively.

As shown in Figure 4-10, the presence of antiferromagnetic regions may be significant for out-of-plane measurements to show hysteresis loops similar to typical loops for normal either ferromagnetic or antiferromagnetic material, with some remnant magnetization. The sequences of the spin switching in the antiferromagnetic region might be expressed as the field is applied in out-of-plane direction. It indicates different functionalities represent independent magnetization of the material.

4.5 **Magnetic Force Microscopy**

A magnetic force microscope is utilized from atomic force microscopy configuration. Unlike contact & non-contact mode AFM, a magnetized tip is used to study magnetic materials, and thus the magnetic interactions between tip and sample are detected. The magnetic force between sample and tip is described as follows:

$$\vec{F} = \mu_0 \left(\vec{m} \cdot \nabla \right) \vec{H} \tag{4.1}$$

where $\vec{m}$ is the magnetic moment of the tip, $\vec{H}$ is the magnetic stray field from the sample surface, and μ_0 is the magnetic permeability of free space.

Since the magnetic stray field from the sample can affect the magnetized state and vice versa of the tip, interpreting the magnetic information from the MFM measurement is needed. For instance, because of the nature of MFM to detect magnetic force gradient, the configuration of the tip magnetization must be known. Typical resolution of 30 nm can be achieved although resolutions as low as 10 to 20 nm are attainable. A potential method of increasing the resolution would involve using an electromagnet on the tip instead of a permanent magnet. Enabling the magnetic tip only when placed over the pixel being sampled could increase the resolution.

AFM / MFM experiments were performed with a Dimension 3100 system [84]. The procedure of MFM imaging utilizes the Interleave and LiftMode option. A tapping cantilever equipped with a ferromagnetic tip is first scanned over the surface of the sample to obtain topographic information. Then, using LiftMode as shown in Figure 4-12, the tip is then raised just above the sample surface. The surface topography is scanned while being monitored for the influence of magnetic forces. These influences are measured using the principle of force gradient detection. In the absence of magnetic forces, the cantilever has a resonant frequency f_0. This frequency is shifted by an amount Δf proportional to vertical gradients in the magnetic forces on the tip. The shifts in resonant frequency tend to be very small, typically in the range 1-50 Hz for cantilevers having a resonant frequency $f_0 \sim 100$Hz. These frequency shifts can be detected three ways: 1) phase detection, which measures the contilever's phase of oscillation relative to the piezo drive; 2) amplitude detection, which tracks variations in oscillation amplitude; and 3) frequency modulation, which directly tracks shifts in resonant frequency. Phase

detection and frequency modulation produce results that are generally used other than amplitude detection.

Before the MFM measurements, the tip should be magnetized with a strong magnet before installing the tip holder on the AFM head. Tips are usually magnetized with the field aligned along the tip axis which is perpendicular to the sample surface. Then, the MFM senses force gradients due to the perpendicular component of the samples' stray field. For the higher sensitivity, electromagnet should be used for the magnetization of the tips.

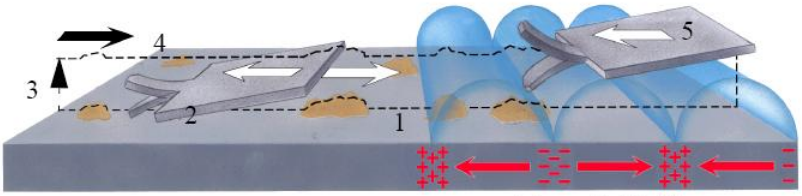

1&2 Cantilever traces surface topography on first trace and retrace.
3 Cantilever ascends to **Lift scan Height**.
4&5 Lifted cantilever profiles topography while responding to magnetic influences on second trace and retrace.

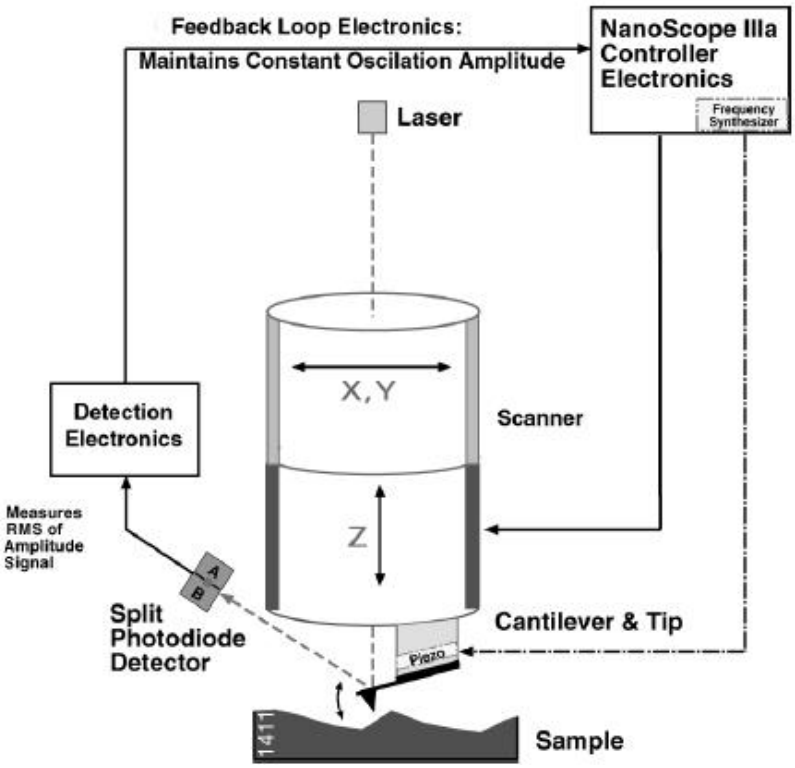

Figure 4-12 The Principles and Schematics of magnetic force microscopy

To detect adequate magnetic sensitivity and eliminate electrical charge effects, graphene sample was mounted as shown in Figure 4-13. From the bottom, the glass for

isolation and magnets to generate uniform magnetization were placed, respectively. Then for electrical isolation, another glass substrate was placed onto the magnet and graphene was on top of the systems. For local electrical isolation, sample was grounded. From optimization process, the measurement system shows adequate magnetic sensitivity to detect and distinguish different magnetic phases with electrical isolation from the surface of the sample to minimize the sensitivity to electric charge effects.

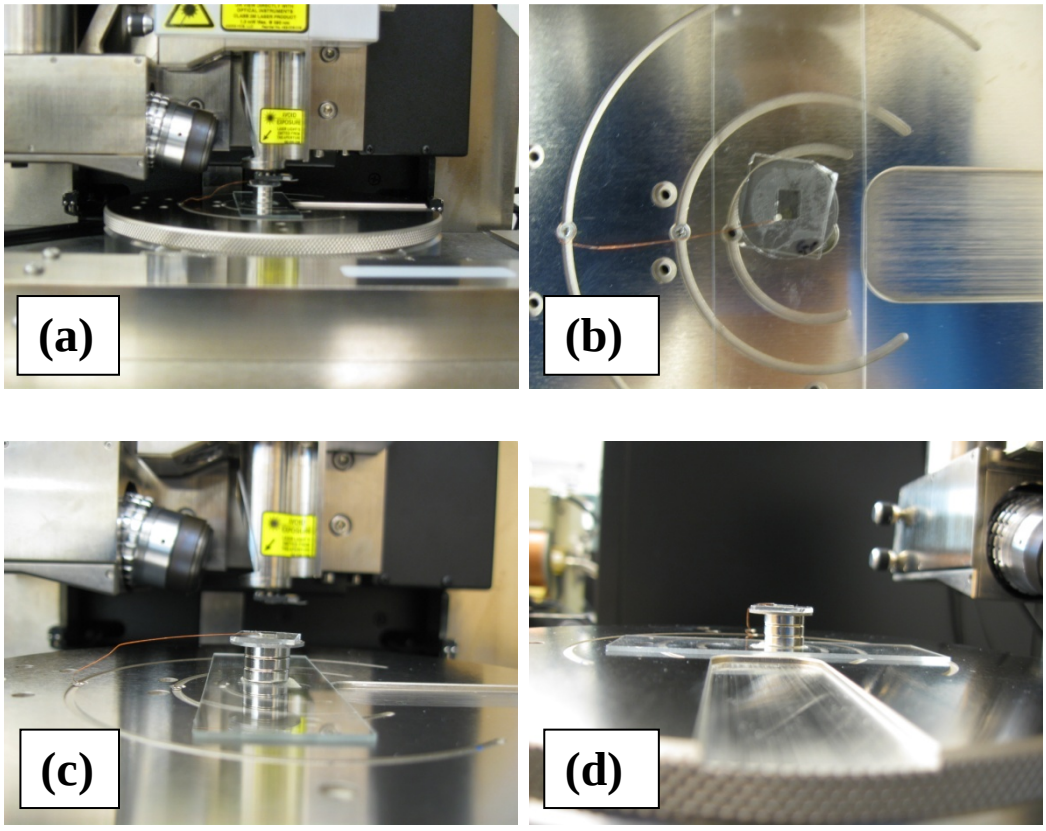

Figure 4-13 The experimental set-up for MFM study of graphene

During experimental measurements, non-contact mode AFM was used. For MFM experiment, a magnetic probe which will be described later (sputter fabricated onto PPP-FMR-50 from Nanosensors^{TM}) with a resonant frequency 45–115 kHz was used [85]. MFM measurements were performed in a dynamic lift-mode operation at a lift-off distance of 30nm over the sample, which was optimized in order to reduce the topographical interference and prevent false imaging. All measurements were taken under open environment and at ambient conditions.

In order to further investigate the nature of the induced magnetism, the effect of the chemical functionality on the EG surface in a combined AFM and MFM study was performed in order to correlate the functionalization with the pronounced increase in magnetism. Simultaneous measurements of the images could match the observed local magnetic properties with the surface topology of the EG. The left and right images in Figure 4-14 show AFM and MFM images, respectively, of a graphene region including patches of functionalized NP-EG. The average height of the functionalized patches was found to be approximately 1 nm; the dark color of the functionalized patches in the MFM image indicates a relatively strong magnetic moment in these regions. The graphene in these patches acts as a soft magnetic material relative to the field generated by the probe (of the order of 2 kOe). It may be noted that the (apparently) pristine areas also shows non-zero magnetic moments in certain regions, though the signal in these areas is substantially weaker (by a factor of 10) than the signal in the functionalized areas.

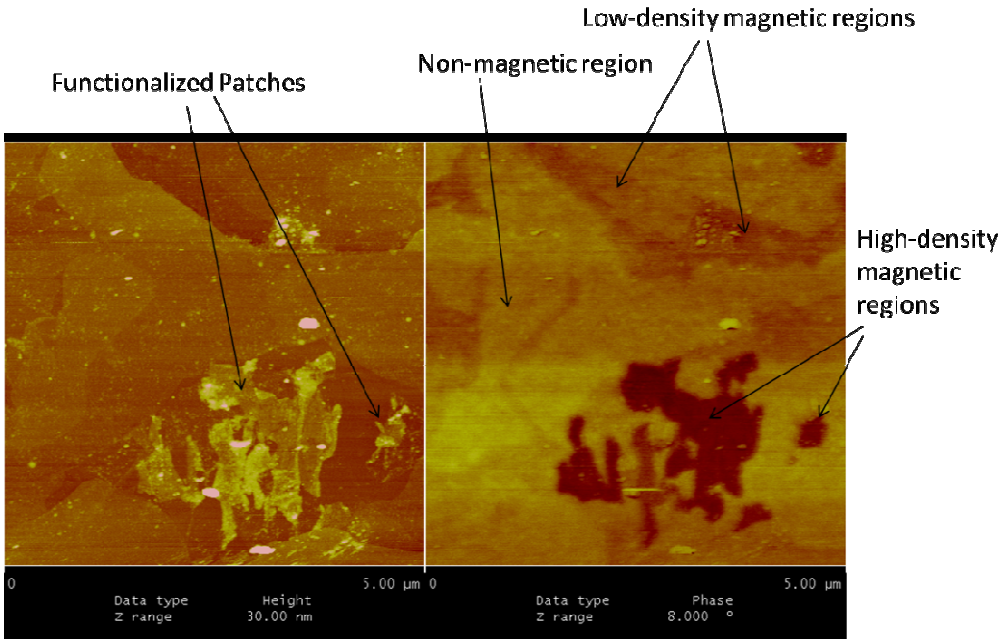

Figure 4-14 (left) and (right) show AFM and MFM images of a 5-micron surface region with functionalized and pristine regions; the average thickness of the functionalized patches is approximately 1 nm.

As shown in Figure 4-15, AFM (L) and MFM (R) images, respectively, of a graphene region show other patches of functionalized NP-EG from another graphene sample. Also, the average height of the functionalized patches was found to be approximately 1 nm.

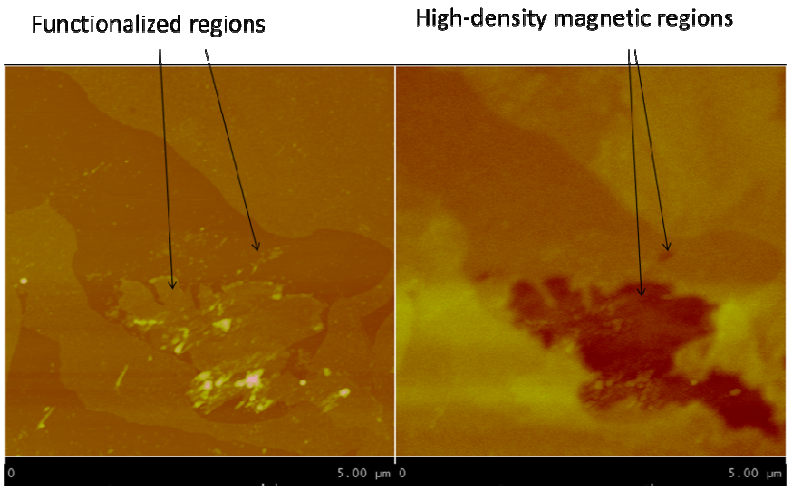

Figure 4-15 AFM (left) and MFM (right) images of a functionalized surface region in sample B. The average thickness of the functionalized patches is approximately 1 nm.

As shown in Figure 4-16, AFM (L) and MFM (R) images for a pristine graphene, respectively; essentially no magnetic signal could be detected.

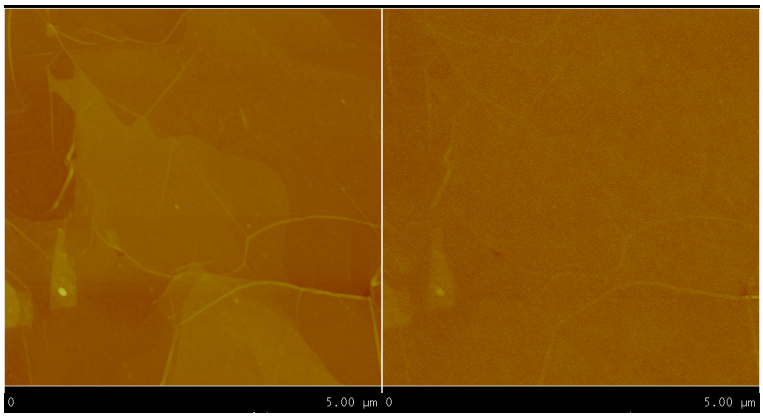

Figure 4-16 AFM (L) and MFM (R) images of a 5 μm region of pristine EG.

In designing and fabricating the MFM probes suitable for this study, the following guidelines should be performed: (i) the probes should have adequate magnetic sensitivity to detect and distinguish different magnetic phases; (ii) the probes should be electrically isolated from the surface of the sample to minimize the sensitivity to electric charge effects [86], (iii) the probe material should have the lowest possible conductivity to minimize the electric charge effects.

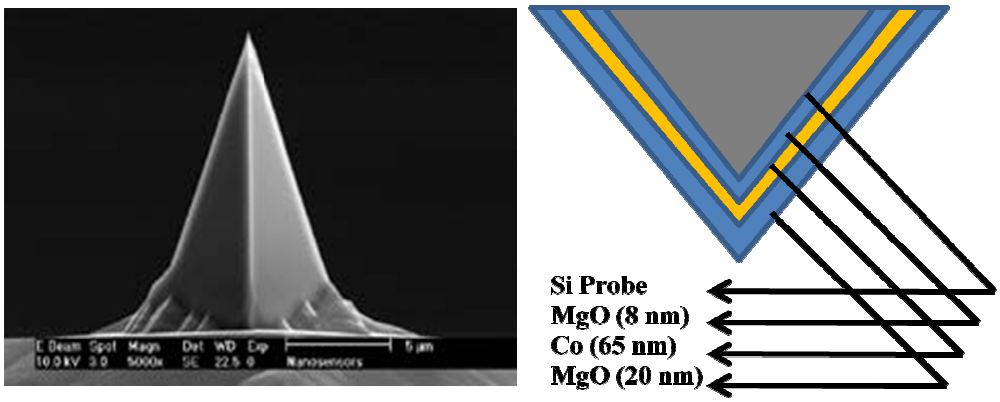

Figure 4-17 Tip composition for MFM of Graphene

Thus, the following procedure was done to coat the silicon probe through sputter deposition: Si probe)/MgO(8nm)/Co(65nm)/MgO(20nm) as shown in Figure 4-17. All the layers were deposited at 5 mtorr Argon processing pressure with a sample rotation of about 30 RPM (for complete and uniform coverage of the cantilever). The MgO and Co

layers were sputter deposited with 270W RF and 57W DC power, respectively. To ensure complete coverage of the front side, the cantilever was placed on a sticky/dry gel platform.

5. Conclusion

5.1 Concluding Remarks

This work focused on the development of finding magnetism of graphene and showed the possibility of room temperature semiconducting ferromagnetism. Chemical functionalization with nitrophenyl group indicates both semiconducting and ferromagnetic behavior. The ferromagnetism is mixed state of ferromagnetism and antiferromagnetism.

From the transport studies, the temperature dependency of graphene was investigated for finding chemical functionality induced semiconducting origin. Second, magnetoresistance of pristine EG & functionalized EG showed ordered MR mechanism. Two distinct and superimposed MR mechanisms was found: first, it is Positive MR: $(1+(\mu H)^2)$ like behavior which is semiconductor with a single carrier type where μ: Mobility and H: Magnetic flux density and the second is Negative MR which is attributed to a giant magnetoresistance effect due to the antiferromagnetic ordering of local spins. Functionalized EG showed negative MR is dominant in whole temperature range and positive MR saturates at higher field instead.

In conclusion, theoretical and experimental works and current results indicated chemical ordering induced ferromagnetism which might be mixed state of ferromagnetic and antiferromagnetic behavior. The correlation between temperature dependent resistance, negative MR, positive MR, and M-H hysteresis loops shows the semiconducting origin of ferromagnetism. The position of the semiconducting energy gap

and the electron effective mass are strongly spin-dependent: low negative field dependence narrows the semiconducting energy gap. This implies that MH hysteresis loops might be associated with the semiconducting phase.

From M-H hysteresis loops results, Figure 5-1illustrates the sequences of the spin switching in the antiferromagnetic region, as the field is applied in in-plane and out-of-plane directions, respectively. Here, it is assumed that the "easy" antiferromagnetic axis is directed normal to the plane. These two loops indeed look like the measured M-H loops.

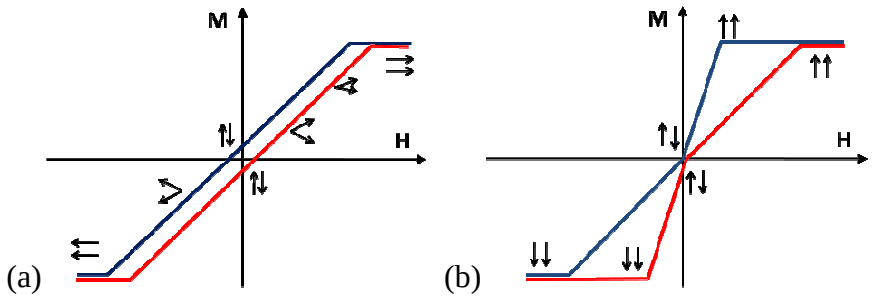

Figure 5-1 Schematics to illustrate the sequences of the spin switching (in the antiferromagnetic regions), as the field is applied in (a) in-plane and (b) out-of-plane directions. The "easy" axis is assumed to be normal to the plane. The red and blue lines show the sides of the loop in the forward and reverse direction of the field, respectively.

Through vibrating sample magnetometry measurements in a temperature range from 2 to 300 K, after chemical functionalization, epitaxially grown graphene samples became room-temperature semiconductor as well as displayed high-density magnetism, with the room-temperature saturation magnetization of the order of 0.1 Bohr magnetons per carbon atom. In addition, the characteristic shape of M-H hysteresis loops indicated a significant contribution of antiferromagnetic regions, with the preferred antiferromagnetic "easy" axis in the normal to the plane direction. The observed anisotropy of the magnetic properties with the two-dimensional nature of graphene sheets was found.

From MFM study, the high density magnetism in the graphene sheet with regions which is coupled both ferromagnetically and antiferromagnetically aligned spins was indicated from the high density functionality patches. It might be increased with high-density chemical functionalization of the EG samples. Room temperature ferromagnetic semiconductor with a saturation magnetization of ~0.1 μ_B per carbon atom (0.5 μ_B per functionality) would be possible from the results. The observed MR indicated field suppression of the spin-dependent scattering at grain or domain boundaries. Carbon atom layers with chemical functionalization shows a granular structure and functionality insert ferromagnetic origins significantly which enhances the negative MR.

5.2 **Directions for Future Applications**

This work has explored the semiconducting ferromagnetism of graphene with functionalization. From the MR signals of the out-of-plane and in-plane components, the anisotropy of spin alignments are observed. These highly anisotropic magnetic properties might be associated with the 2D nature of graphene samples. Towards 2D semiconducting ferromagnet, it would be possible through Aryl radical functionalization of epitaxial graphene since the electronic & magnetic properties depends on the coverage of chemical functionalization.

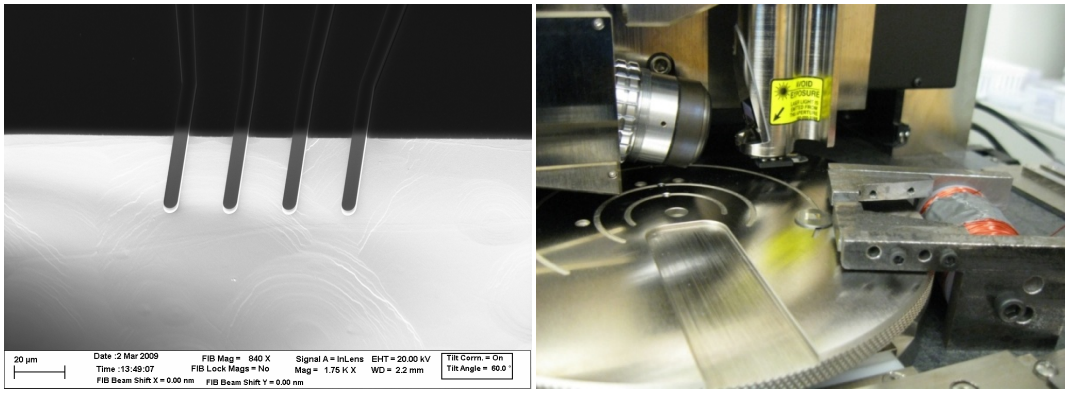

Figure 5-2 Local 4-Probe Measurement tips (L) with local field generator (R) via scanning probe microscopy.

Critical Research Fulfillments for the future studies include magnetism and semiconducting properties of functionalization induced graphene based on the coverage

of chemical functionality. The dependency of the degree of functionality should be studied to find the nature of magnetism and semiconducting origin. As shown in Figure 5-2, local 4-Probe Measurement for local magnetic fields to find local MR effects could be investigated. Also, it is special time to pioneer device fabrication of graphene magnetic semiconductor. Last, strength of materials studies would be done via tribology research of chemical functionality and graphene itself.

References

1. J. D. Meindl, Q. Chen, and J. A. Davis, "Limits on Silicon Nanoelectronics for Terascale Integration," *Science* **293**, 2044-2049 (2001)

2. *The International Technology Roadmap for Semiconductors (ITRS)* (Semiconductor Industry Association, San Jose, CA, 2008)

3. M. Kanellos, "New Life for Moore's Law," *CNET News*, CBS Interactive Inc., Retrieved from http://news.cnet.com/New-life-for-Moores-Law/2009-1006_3-5672485.html (2005)

4. P. Gelsinger, "Moore's Law: "We See No End in Sight," Says Intel's Pat Gelsinger," *SYS-CON Media*, Retrieved from http://websphere.sys-con.com/node/557154 (2008)

5. S. A. Wolf, D. D. Awschalom, R. A. Buhrman, J. M. Daughton, S. von Molnar, M. L. Roukes, A. Y. Chtchelkanova, D. M. Treger, "Spintronics: a spin-based electronics vision for the future," *Science* **294**, 1488-95 (2001)

6. F. Maccherozzi, M. Sperl, G. Panaccione, J. Minar, S. Polesya, H. Ebert, U. Wurstbauer, M. Hochstrasser, G. Rossi, G. Woltersdorf, W. Wegscheider, C. H. Back, "Evidence for a magnetic proximity effect up to room temperature at Fe/(Ga, Mn)As interfaces," *Phys. Rev. Lett*. **101**, 267201 (2008)

7. H. Munekata, H. Ohno, S. von Molnár, Armin Segmüller, L. L. Chang, L. Esaki, "Diluted magnetic III-V semiconductors," *Phys. Rev. Lett*. **63**, 1849 (1989)

8. C. Berger, Z. Song, T. Li, X. Li, A. Y. Ogbazghi, R. Feng, Z. Dai, A. N. Marchenkov, E. H. Conrad, P. N. First, W. A. deHeer *J. Phys. Chem. B* **108**, 19912 (2004)

9. K. S. Novoselov, A. K. Geim, S. V. Morozov, D. Jiang, Y. Zhang, S. V. Dubonos, I. V. Grigorieva, A. A. Firsov, “Electric field effect in atomically thin carbon films,” *Science* **306** (5696), 666-9 (2004)

10. Y.-W. Tan, Y. Zhang, H. L. Stormer, P. Kim, “Temperature-dependent electron transport in graphene,” *Eur. Phys. J. Special Topics* **148**, 15-8 (2007)

11. K. I. Bolotin, K. J. Sikes, J. Hone, H. L. Stormer, P. Kim, “Temperature-dependent transport in suspended graphene,” *Phys. Rev. Lett*. **101**, 096802 (2008)

12. N. Tombros, et al., "Electronic spin transport and spin precession in single graphene layers at room temperature," *Nature* **448**, 571–575 (2007)

13. A. K. Geim, K. S. Novoselov, “The rise of graphene,” *Nat. Mater*. **6**, 183 - 191 (2007)

14. B. Fuller, S. Sadao, “Geodesic Dome,” US Pavilion at Expo '67 Retrieved from http://en.wikipedia.org/wiki/Geodesic_dome (1967)

15. G. Tegos, T. Demidova, D. Arcila-Lopez, H. Lee, T. Wharton, H. Gali, M. Hamblin, “Cationic Fullerenes Are Effective and Selective Antimicrobial Photosensitizers,” *Chem. & Bio.* **12** (10), 1127–1135 (2005)

16. L. X. Zheng et al., “Ultralong Single-Wall Carbon Nanotubes,” *Nat. Mater*. **3**, 673 - 676 (2004)

17. M. Ströck, Image Retrieved from Wikimedia (2009)

18. J. C. Meyer, A. K. Geim, M. I. Katsnelson, K. S. Novoselov, T. J. Booth, S. Roth, “The structure of suspended graphene sheets,” *Nature* **446**, 60-63 (2007)

19. K. S. Kim, Y. Zhao, H. Jang, et al., “Large-scale pattern growth of graphene films for stretchable transparent electrodes,” *Nature* **457**, 706-710 (2009)

20. K. S. Novoselov, D. Jiang, F. Schedin, T. J. Booth, V. V. Khotkevich, S. V. Morozov, A. K. Geim, “Two-dimensional atomic crystals,” *Proc. Nat’l. Acad. Sci. U. S. A.* **102** (30), 10451-10453 (2005)

21. S. Park, R. S. Ruoff, “Chemical methods for the production of graphenes,” *Nat. Nanotech.* **4**(4), 217–224 (2009)

22. W. A. de Heer, C. Berger, X. S. Wu, P. N. First, E. H. Conrad, X. B. Li, T. B. Li, M. Sprinkle, J. Hass, M. L. Sadowski, M. Potemski, G. Martinez, “Epitaxial Graphene,” *Solid State Commun.* **143**, 92-100 (2007)

23. C. Berger, Z. M. Song, X. B. Li, X. S. Wu, N. Brown, C. Naud, D. Mayou, T. B. Li, J. Hass, A. N. Marchenkov, E. H. Conrad, P. N. First, W. A. de Heer, “Electronic Confinement and Coherence in Patterned Epitaxial Graphene,” *Science* **312** (5777), 1191-1196 (2006)

24. G. M. Rutter, J. N. Crain, N. P. Guisinger, T. Li, P. N. First, J. A. Stroscio, “ Scattering and Interference in Epitaxial Graphene,” *Science* **317** (5835), 219 - 222 (2007)

25. W. S. Hummers Jr., R. E. Offeman, “Preparation of Graphitic Oxide,” *J. Am. Chem. Soc.* **80** (6), 1339 (1958)

26. B.C. Brodie, “Sur le poids atomique du graphite,” *Ann. Chim. Phys.* **59**, 466-472 **(**1860**)**

27. C. Schafhaeutl, “On the combination of carbon with silicon and iron, and other metals, forming the different species of cast iron, steel, and malleable iron,” *Phil. Mag.* **16**, 570–590 (1840)

28. H. Shioyama, “Cleavage of graphite to graphene,” *J. Mater. Sci. Lett.* **20**, 499-500 (2001)

29. H. He, J. Klinowski, M. Forster, A. Lerf, “A new structural model for graphite oxide,” *Chem. Phys. Lett.* **287**, 53–56 (1998)

30. H. He, T. Riedl, A. Lerf, J. Klinowski, “Solid-state NMR studies of the structure of graphite oxide,” *J. Phys. Chem.* **100**, 19954–19958 (1996)

31. A. Lerf, H. He, M. Forster, J. Klinowski, “Structure of graphite oxide revisited,” *J. Phys. Chem. B* **102**, 4477–4482 (1998)

32. W. Cai et al., “Synthesis and solid-state NMR structural characterization of 13C-labeled graphite oxide,” *Science* **321**, 1815–1817 (2008)

33. A. Buchsteiner, A. Lerf, J. Pieper, “Water dynamics in graphite oxide investigated with neutron scattering,” *J. Phys. Chem. B* **110**, 22328–22338 (2006)

34. S. Stankovich et al., “Stable aqueous dispersions of graphitic nanoplatelets via the reduction of exfoliated graphite oxide in the presence of poly(sodium 4-styrenesulfonate),” *J. Mater. Chem.* **16**, 155–158 (2006)

35. I. Jung et al., “Simple approach for high-contrast optical imaging and characterization of graphene-based sheets,” *Nano Lett.* **7**, 3569–3575 (2007)

36. H. P. Boehm, A. Clauss, G. O. Fischer, U. Hofmann, “Das Adsorptionsverhalten sehr dunner Kohlenstoff-Folien,” *Anorg. Allg. Chem.* **316**, 119–127 (1962)

37 . H. P. Boehm, M. Eckel, W. Scholz, “Uber den Bildungsmechanismus des Graphitoxids,” *Anorg. Allg. Chem.* **353**, 236–242 (1967)

38. D. A. Dikin et al., “Preparation and characterization of graphene oxide paper,” *Nature* **448**, 457–460 (2007)

39. D. Li, M. B. Muller, S. Gilje, R. B. Kaner, G. G. Wallace, “Processable aqueous dispersions of graphene nanosheets,” *Nat. Nanotech.* **3**, 101–105 (2008)

40. Y. Xu, H. Bai, G. Lu, C. Li, G. Shi, “Flexible graphene films via the filtration of water-soluble noncovalent functionalized graphene sheets,” *J. Am. Chem. Soc.* **130**, 5856–5857 (2008)

41. S. Park et al., “Aqueous suspension and characterization of chemically modified graphene sheets,” *Chem. Mater.* **20**, 6592–6594 (2008)

42. H. Chen, M. B. Muller, K. J. Gilmore, G. G. Wallace, D. Li, “Mechanically strong, electrically conductive, and biocompatible graphene paper,” *Adv. Mater.* **20**, 3557–3561 (2008)

43. Y. Si, E. T. Samulski, “Synthesis of water soluble graphene,” *Nano Lett.* **8**, 1679–1682 (2008)

44. G. Eda, G. Fanchini, M. Chhowalla, “Large-area ultrathin films of reduced graphene oxide as a transparent and flexible electronic material,” *Nat. Nanotech.* **3**, 270–274 (2008)

45 X. Wang, L. Zhi, K. Müllen, “Transparent, conductive graphene electrodes for dye-sensitized solar cells,” *Nano Lett.* **8**, 323–327 (2008)

46. A. Reina, X. Jia, J. Ho, D. Nezich, H. Son, V. Bulovic, M. S. Dresselhaus, J. Kong, "Large Area, Few-Layer Graphene Films on Arbitrary Substrates by Chemical Vapor Deposition," *Nano Lett.* **9** (1), 30-35 (2009)

47. A. N. Obraztsov, "Chemical vapour deposition: Making graphene on a large scale," *Nat. Nanotech.* **4**, 212 - 213 (2009)

48. E. Bekyarova et al., "Chemical Modification of Epitaxial Graphene: Spontaneous Grafting of Aryl Groups," *J. Am. Chem. Soc.* **131**, 1336-1337 (2009)

49. E. Bekyarova, M. E. Itkis, P. Ramesh, R. C. Haddon, "Chemical Approach to the Realization of Electronic Devices in Epitaxial Graphene," *Phys. Stat. Sol. RRL* **3**, 184-186 (2009)

50. J. Hong et al., Unpublished

51. O. V. Yazyev L. Helm, "Defect-Induced Magnetism in Graphene," *Phys Rev. B* **75**, 125408 (2007)

52. F. Wenner, "A method of measuring earth resistivity," *Bull. of the Bureau of Standards* **12**, 469-478 (1912)

53. D. K. Schroder, "Semiconductor Material and Device Characterization," 3rd Edition IEEE Press, John Wiley & Sons, Inc., Hoboken, New Jersey (2006)

54. QD Application Note, "Magnetometry by means of Hall micro-probes," Quantum Design PPMS *1084-701 Rev. A0* (2007)

55. E. H. Hwang, S. Adam, S. Das Sarma, "Carrier Transport in Two-Dimensional Graphene Layers," *Phys. Rev. Lett.* **98**, 186806 (2007)

56. J.-H. Chen, C. Jang, S. Adam, M. S. Fuhrer, E. D. Williams, M. Ishigami, "Charged-impurity scattering in graphene," Nat. Phys. 4, 377 - 381 (2008)

57. K. Nomura, A. H. MacDonald, "Quantum Hall Ferromagnetism in Graphene," *Phys. Rev. Lett.* **96**, 256602 (2006)

58. S. V. Morozov, K. S. Novoselov, M. I. Katsnelson, F. Schedin, D. C. Elias, J. A. Jaszczak, A. K. Geim, "Giant Intrinsic Carrier Mobilities in Graphene and Its Bilayer," *Phys. Rev. Lett.* **100**, 016602 (2008)

59. E. H. Hwang, S. Das Sarma, "Acoustic phonon scattering limited carrier mobility in two-dimensional extrinsic graphene," *Phys. Rev. B* **77**, 115449 (2008)

60. F. T. Vasko, V. Ryzhii, "Voltage and temperature dependencies of conductivity in gated graphene," *Phys. Rev. B* **76**, 233404 (2007)

61. T. Stauber, N. M. R. Peres, F. Guinea, "Electronic transport in graphene: A semiclassical approach including midgap states," *Phys. Rev. B* **76**, 205423 (2007)

62. J. H. Chen, C. Jang, S. Xiao, M. Ishigami, M. S. Fuhrer, "Intrinsic and extrinsic performance limits of graphene devices on SiO2," *Nat. Nanotech.* **3**, 206 - 209 (2008)

63. E. Stolyarova, K. T. Rim, S. Ryu, J. Maultzsch, P. Kim, L. E. Brus, T. F. Heinz, M. S. Hybertsen, G. W. Flynn, "High-resolution scanning tunneling microscopy imaging of mesoscopic graphene sheets on an insulating surface," *Proc. Natl. Acad. Sci. U.S.A.* **104**, 9209-9212 (2007)

64. M. Ishigami, J. H. Chen, W. G. Cullen, M. S. Fuhrer, E.D. Williams, "Atomic Structure of Graphene on SiO2," *Nano Lett.* **7**, 1643 (2007)

65. F. Guinea, M. I. Katsnelson, M. A. H. Vozmediano, "Midgap states and charge inhomogeneities in corrugated graphene," *Phys. Rev. B* **77**, 075422 (2008)

66. J. Martin, N. Akerman, G. Ulbricht, T. Lohmann, J. H. Smet, K. von Klitzing, A. Yacoby, "Observation of electron–hole puddles in graphene using a scanning single-electron transistor," *Nat. Phys.* **4**, 144-148 (2008)

67. K. I. Bolotin, K. J. Sikes, Z. Jiang, M. Klima, G. Fudenberg, J. Hone, P. Kim, H. L. Stormer, "Ultrahigh electron mobility in suspended graphene," *Solid State Commun.* **146**, 351-355 (2008)

68. W. Thomson, "On the Electro-Dynamic Properties of Metals," *Proc. R. Soc. Lond.* **8**, 546 (1857)

69. M. N. Baibich , J. M. Broto, A. Fert, F. Nguyen Van Dau, F. Petroff, P. Eitenne, G. Creuzet, A. Friederich, J. Chazelas, "Giant Magnetoresistance of (001)Fe/(001)Cr Magnetic Superlattices," *Phys. Rev. Lett.* **61** (21), 2472–2475 (1988)

70. G. H. Jonker, J. H. Van Santen, "Ferromagnetic compounds of manganese with perovskite structure," *Physica* **16**, 337-349 (1950)

71. M. Julliere, "Tunneling between ferromagnetic films," *Phys. Lett.* **54A**, 225–226 (1975)

72. P. Grünberg, R. Schreiber, Y. Pang, M. B. Brodsky, H. Sowers, "Layered magnetic structures: evidence for antiferromagnetic coupling of Fe layers across Cr interlayers," *Phys. Rev. Lett.* **57** (19), 2442-2445 (1986)

73. M. N. Baibich , J. M. Broto, A. Fert, F. Nguyen Van Dau, F. Petroff, P. Eitenne, G. Creuzet, A. Friederich, J. Chazelas, "Giant magnetoresistance of (001)Fe/(001)Cr magnetic superlattices," *Phys. Rev. Lett*. **61** (21), 2472-5 (1988)

74. A. E. Berkowitz, J. R. Mitchell, M. J. Carey, A. P. Young, S. Zhang, F. E. Spada, F. T. Parker, A. Hutten, G. Thomas, "Giant magnetoresistance in heterogeneous Cu-Co alloys," *Phys. Rev. Lett.* **68** (25), 3745-8 (1992)

75. G. Peleckis, X. L. Wang, S. X. Dou, P. Munroe, J. Ding, B. Lee, "Giant positive magnetoresistance in Fe doped In2O3 and InREO3 (RE=Eu, Nd) composites," *J. Appl. Phys*. **103**, 07D113 (2008)

76. G. M. Rutter, J. N. Crain, N. P. Guisinger, P. N. First, J. A. Stroscioa, "Structural and electronic properties of bilayer epitaxial graphene," *J. Vac. Sci. Technol. A* **26** (4) 938-943 (2008)

77. STM module from Veeco Inc. (http://www.veeco.com)

78. Dimension 3100 Manual from Veeco

79. R. A. Wood, M. H. Lewis, M. R. Lees, S. M. Bennington, M. G. Cain, N. Kitamura, "Ferromagnetic fullerene," *J. Phys.: Condens. Matter* **14** (22), L385-L391 (2002)

80. A. Mahajan, A. Rangwala, "Electricity and Magnetism," 419 (1989)

81. S. Niyogi, E. Bekyarova, M. E. Itkis, J. L. McWilliams, M. A. Hamon, R. C. Haddon, "Solution Properties of Graphite and Graphene," *J. Am. Chem. Soc.* **128**, 7720-7721 (2006)

82. A product of Quantum Design Corporation (http://www.qdusa.com)

83. VSM-PPMS application note

84. MFM module from Veeco Inc., (http://www.veeco.com)

85. A product (PPP-FMR-50) from Nanosensors^{TM} (http://www.nanosensor.com)

86. N. Amos, R. Ikkawi, R. C. Haddon, D. Litvinov, S. Khizroev, “Controlling multi-domain states to enable sub-10-nm magnetic force microscopy,” *Appl. Phys. Lett*. **93**, 203116-203118 (2008)